Development and Hover Testing of the Active Elevon Rotor

Mark V. Fulton
mark.v.fulton@us.army.mil

Nili P. Gold
nili.gold@us.army.mil

Gavin E. Nielsen*
gavin.nielsen@gmail.com

Mohammadreza H. Mansur
mohammadreza.mansur@us.army.mil

Mark B. Tischler
mark.tischler@us.army.mil

Aeroflightdynamics Directorate (AMRDEC)
US Army Research, Development, and Engineering Command
Ames Research Center, Moffett Field, California

*Graduate Student Intern, NASA Education Associates Program
California State University, Chico

and

David B. Domzalski
domzalskimach@att.net
Domzalski Machine
Prescott, Arizona

ABSTRACT

The Active Elevon Rotor (AER) is a 12.96 ft. diameter rotor with two on-blade elevons on each blade. Each elevon is a 15% chord, 8% span, plain, trailing-edge flap actuated by a piezoceramic-based conformal actuator. Development of the rotor and support systems has been completed and is documented, especially regarding the actuation system, blades, test stand, and controls. Development of two control algorithms – classical and Model Predictive Control (MPC) – is described for elevon position control. Two-bladed active rotor testing was conducted in hover, including elevon frequency dwells and logarithmic frequency sweeps, and initial test results are documented, especially from elevon and blade load measurements. Actuation system performance was good (±2° thru 1025 RPM), but actuator reliability at the design electric voltage limits was poor, and the actuation assembly flexure properties need improvement. The test stand was stiffened to ensure aeromechanical stability. The measured control bandwidth was 1.3/rev. The measured blade torsion frequency was found to be significantly lower than predicted.

NOTATION

b	number of blades
B#	blade number #
c	blade chord, 5.670 in.
C	blade chord bending moment (or CM)
CAEA	conformal actuator and elevon assembly
CAT	conformal actuator technology
F	blade flap bending moment (or FM) OR Hankel matrix of the system
Fc	cutoff frequency (in Hz)
hpp	half peak-to-peak
$IBB1$	inboard elevon, blade #1
$IBB3$	inboard elevon, blade #3
M	Mach number
$OBB1$	outboard elevon, blade #1
$OBB3$	outboard elevon, blade #3
r	reference sent to controller (setpoint)
rps	radians per second
R	rotor radius, 6.48 ft. (77.76 in)
T	blade torsion moment (or TM)
$u\ or\ U$	command sent from controller
x	state vector (state-space)
Y	plant output (truth)

α	angle of attack
$\beta_{\#}$	flap mode number #
$\zeta_{\#}$	lag mode number #
$\phi_{\#}$	torsion mode number #
Φ	Toeplitz matrix of the system
Ω_O	nominal rotor speed, 1070 RPM

INTRODUCTION

The need for improved helicopter rotor aeromechanics has led to a wide range of investigations. Concepts and developments are typically aimed at reducing vibration, improving rotor performance, and/or reducing blade-vortex interaction (BVI) or in-plane noise. These efforts include a wide variety of active rotor concepts. Examples include higher harmonic control (HHC) of the swashplate (Ref. 1), individual blade control (IBC) of rotor pitch links (Refs. 2 and 3), and various on-blade controls – such as active flaps (Refs. 4, 5, 6, 7, and 8) and active twist (Ref. 9) – that can utilize IBC type algorithms.

The Active Elevon Rotor (AER) was a joint Army/NASA project, originally planned for a wind tunnel test, primarily to demonstrate reduced vibration, but also to quantify the active rotor's ability to reduce rotor power and noise. This project was initiated as a Focus Demo of the Aeromechanics Steering Committee of the AMRDEC. The

primary goal was the acquisition of aeromechanics research data – especially blade structural loads, hub deflections, and hub loads – to quantify elevon control effectiveness. Wind tunnel testing was to include typical and limiting flight conditions for advance ratio and blade loading (C_T/σ). Secondary goals were the development and demonstration of an active rotor, to advance the technology and quantify the resulting performance of the actuation system; and to demonstrate the performance of existing or advanced control algorithms. The design objective was to reduce the vibratory hub loads by 80% in forward flight.

The AER project selected a dual-elevon configuration – two independently controlled elevons per blade – with each elevon actuated by a conformal actuation system developed under an Army Small Business Innovation Research (SBIR) contract (DAAH10-99-C-0022). Each elevon is a 15% chord, 8% span, plain, trailing-edge flap actuated by a piezoceramic-based actuator. The plain control surface – without aerodynamic balance – was selected to provide a clean aerodynamic surface with low drag increments, even though this increases the aerodynamic hinge moment that must be overcome by the actuation system. Conformal actuation was developed to provide good aerodynamic characteristics and to minimize the number of moving parts and wear for reduced maintenance. The dual-elevon configuration was expected to provide sufficient control authority for a good experimental investigation. It was largely selected because the presence of two elevons should allow for increased experimental flexibility. In principle, a spanwise separation between the elevons should allow for tailored excitation of different blade modes, although this comes at the expense of increased finite span aerodynamic losses. The aeromechanics design process was documented in Refs. 10 and 11.

Much of the literature shows application of Higher-Harmonic Control architectures to active rotors control problems (Refs. 12 and 13) due to a good match of application needs for performing steady-state control of harmonics and rejecting the steady-state disturbance harmonics. For AER, a significant effort was made to develop a time-domain controller, to enable other aspects of active rotor reference tracking (such as frequency sweeps and other unsteady reference trajectories) as well as to quantify the extent to which transient response might be improved.

The AER control development was focused on elevon position control. The effort included the development of two sets of actuation system plant models based on frequency sweep data. Then two sets of time-domain controllers were developed, one based on classical approaches and another using Model Predictive Control (MPC) to explore the application of a modern control architecture to this problem. The classical controller was a simple design based on control elements that are well understood. The MPC architecture was selected due to its ability to make better explicit use of

plant knowledge a priori and the relatively fixed, linear nature of its formulation, for robustness/stability.

The paper contains two main parts: 1) development, and 2) testing and results. The development effort is divided into four sections: 1) Rotor Development and Properties, 2) Test Stand Description, 3) Power System Description, and 4) Controls Development. These sections are used to describe the hardware systems, their major properties, and significant aspects of the development effort.

The second part of the paper describes the tests performed and the results. Testing primarily included experiments performed at Domzalski Machine and the Aeroflightdynamics Directorate (AFDD). These tests included bench tests, a small diameter centrifugal test, and airfoil tests. Finally, rotor tests were conducted in the AFDD Hover Chamber – passive blade spins (with two and four blades), and an active rotor hover test (with two blades). The testing and results are divided into six sections: 1) Actuator and CAEA (Conformal Actuator and Elevon Assembly) Testing, 2) Aeromechanical Stability, 3) CAEA Flexure Development and Experience, 4) Hover Test Measurements and Operations, 5) Controls Results, and 6) Aeromechanics Results. The rotor testing was primarily to verify the engineering adequacy of the newly developed hardware. A secondary hover objective was the acquisition of preliminary research data, especially actuator performance, controller performance, elevon control authority, and blade dynamics.

The paper concludes with sections on Future Work and Concluding Remarks.

ROTOR DEVELOPMENT AND PROPERTIES

Rotor Description

Each Active Elevon Rotor (AER) blade includes two on-blade elevons, each of which is part of a Conformal Actuator and Elevon Assembly (CAEA) bonded in a recess on the lower surface of the blade (Figure 1). Each elevon is a 15% chord, plain, trailing-edge flap, with a span of 6.25 inch (8% R). They are centered at 64% R (inboard, IB) and 90% R (outboard, OB). The rotor has a hover tip Mach number of 0.65 (Ω_0 = 1070 RPM), a diameter of 12.96 feet, and a blade chord of 5.67 inches; in these respects, the rotor is identical to an ideally scaled 27% Apache (Ref. 14). The planform is rectangular and the blade has a linear twist rate (of -10 deg/R) outboard of the root cutout. A single airfoil is used for the entire blade length – a VR-18 with a 4% chord, -3° trailing-edge tab.
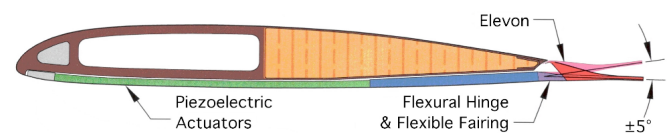

Figure 1. Active cross-section and CAEA, schematic.

The planform of the AER design is depicted in Figure 2, and the rotor design goals are listed in Table 1. The structural design concept developed by Advanced Technologies, Inc. (ATI) yields nearly uniform structural properties along the length of the blade, except for an appreciable mass (and pitching inertia) increment near each active section because of the presence of the actuator. The uniform passive blade stiffness targets, other than torsion stiffness, were taken from the ideally scaled 27% Apache properties. The torsion stiffness design *target* was selected to produce a first torsion natural frequency of 3.3/rev. (Based on results described in Refs. 10 and 11, $\omega_{\varphi 1}$ = 3.3/rev was selected as being "near optimal" and "more interesting" from a blade deformation perspective.) The resulting blade was rather heavy, with a Lock Number of 5.3.
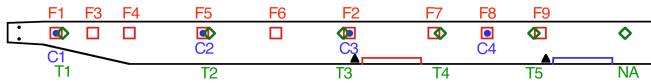
**Figure 2. Blade planform and strain gage bridge locations (Flap, Chord, and Torsion moments).**

Table 1. Rotor design goals.

| Description	Variab.	Value
No. of Blades	b	4
Rotor Radius, ft	R	6.48 (77.76 in)
Airfoil Chord, in	c	5.670
Solidity (bc/πR)	σ	0.0928
Twist, Linear, deg	θ_{pt}	-10
Feathering & Twist Axes		0.27c
Blade Elastic Axis		0.20c
Blade Center of Gravity		0.263c
Blade Tensile Axis		0.263c
Flap-Lag Hinge Loc., in	e	2.97 (0.0382R)
Blade Grip Loc., in	r_g	10.530 (0.1354R)
Root Cutout Loc., in	r_c	22.17 (0.2851R)
Elevon Chord, Plain, in	c_δ	0.850 (0.15c)
Elevon Motion, deg	δ	±5.0 at r_δ = 0.86R
Density, Air, slug/ft³	ρ_o	0.002377
Rotor Speed (nom.), RPM	Ω_o	1,070 (17.83 Hz)
Mach No. (nom.), hover	M_{tip}	0.6504

PZT Actuators

Each CAEA has four CAT (Conformal Actuator Technology) actuators. The CAT actuators (Figure 3) have active elements made of a piezoceramic material from CTS (3203HD). This material is lead zirconate titanate, a PZT 5H HD (high density) material, Navy Type VI. Each CAT is composed of two 2.85 x 2.85 x 0.005 inch sheets of PZT, surrounded by sheets of Stitts Poly-Fiber (FAA PMA)/epoxy, designed to provide some prestress without adding significant stiffness to the actuator (Figure 4). The PZT sheets are poled face-to-face or back-to-back. The CATs are fabricated in a heated, closed mold, that is curved to match the contour of the airfoil lower surface. Initial SBIR design and testing was performed for an applied voltage of 190 ± 300 V, which is equivalent to a nominal

electric field of 38 ± 60 V/mil, or -22 to +98 V/mil. As will be discussed later, such high electric fields did not produce high actuator reliability (life) for the current actuator hardware.
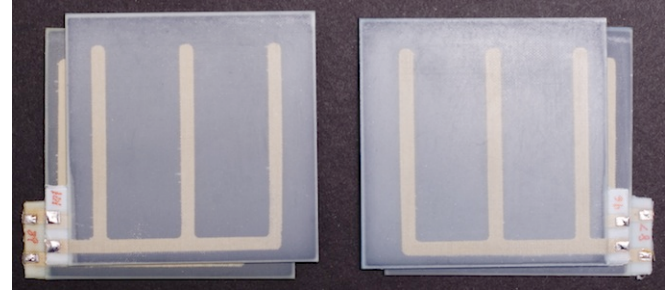

Figure 3. Four CAT actuators.
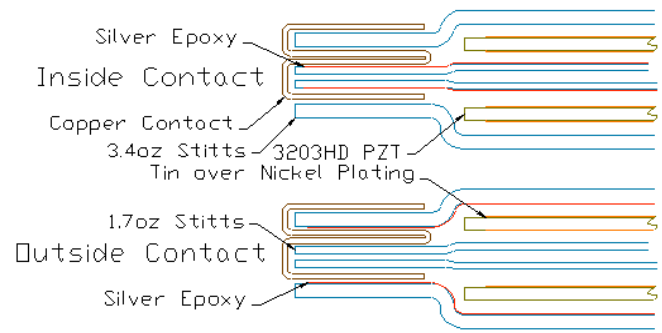
Figure 4. CAT actuator layers, schematic.

The PZT material strains in response to an applied electric field. Here, the d_{31} coupling coefficient is being used. So, the electric field is applied across the thickness, and the resulting useful strain is in the plane of the material, especially the chord-wise strain. The relation between electric field and strain is nonlinear, including hysteresis and material saturation effects. To obtain a useful bulk inverse piezoelectric response, the material is poled in one direction (through the thickness). Consequently, the applied electric field (voltage per unit thickness) limit is significantly larger in the direction of polarization than in the opposite direction. The limit in the direction of polarization is typically governed by electrical failure (e.g. dielectric strength limits). In the opposite direction, excessive voltage typically leads to increased domain switching, thus producing larger electric currents and heat, which can damage the material. As will be later described, an electric power system was developed to apply larger voltages in the direction of polarization, thus extracting larger peak-to-peak strain from the material.

## Conformal Actuator and Elevon Assembly (CAEA)

As previously seen in Figure 1 and Figure 2, each AER Blade includes two on-blade elevons, each of which is part of a Conformal Actuator and Elevon Assembly (CAEA). Figure 5 shows a (5.67 inch chord) demonstrator that includes a CAEA bonded to the lower surface. This photo also shows a separate (single-wide) CAEA, which reveals the actuators (green portion towards the leading edge), three

small electrodes (pointing towards the demonstrator), composite links (between the actuators and the flexural hinge), and the elevon, which includes an upper surface fairing (Figure 1). The upper and lower layers are joined at the leading edge by a LE Joiner, made of tungsten. This part provides a cantilever boundary condition and moves the assembly c.g. forward. The on-blade conformal actuator technology (CAT) was developed by Domzalski Machine under an Army SBIR, Refs. 15 and 16, and was developed for AER by Domzalski Machine under a subcontract to ATI.
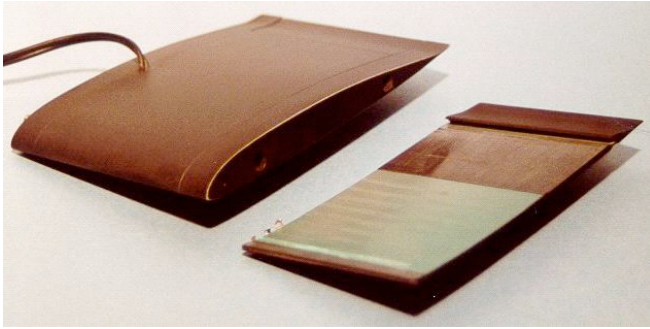
Figure 5. Demonstrator and separate CAEA.

The CAEA mechanical principles are shown in Figure 6. In this figure, two actuators (yellow) act in opposition to deflect a control surface (red). The actuators (one upper and one lower) are separated from one another and from the supporting structure (diagonal blue) by a soft elastomer (vertical brown). The AER implementation differs from these details in the following ways: 1) the lower actuator (plus some fill/fair) is the lower surface of the AER airfoil, 2) the control surface elastic deformation is localized to a flexural hinge, 3) a light weight composite link is placed between the actuator and the flexure, and 4) the elevon shape approximates a plain elevon (Figure 1). Note that use of a flexural hinge means that the elevon motion is not a pure rotation. Instead, the flexure/elevon motion includes a small vertical deflection, approximately 0.006 inch up for +10° (trailing edge down) rotation and 0.008 inch down for –10° rotation.
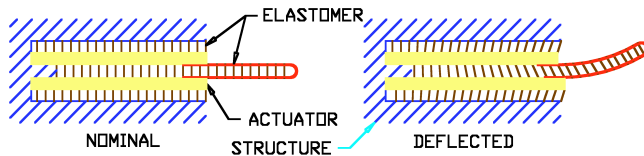
Figure 6. CAEA functional concept (Ref. 15).

The operational requirements for the CAEA were established to satisfy rotor testing in a wind tunnel. The radial acceleration was for 113% RPM, at 0.90R, which corresponds to 2,904 g. For actuator performance, the free-stream Mach number was to be 0.56 (the Mach number at 0.86R in hover). The actuator was to produce zero elevon deflection for a static angle of attack (α) of 6° plus an oscillatory elevon deflection (δ) of ±5°. (The actuator has a free (unloaded) deflection of about ±10°.) Blade structural

loads are not significant for CAEA loading, since the CAEA is isolated from the blade by the soft elastomer.

Each AER CAEA includes two actuator subassemblies, with one elevon that spans the entire CAEA. Since each actuator subassembly is composed of two CAT actuators, one CAEA is composed of four CAT actuators (Figure 3), two upper and two lower. Between the actuator/link subassemblies is a no-PZT zone, where fill is used to recover the airfoil profile. (The foundational actuator assembly (Figure 5) is called a "single wide", and the AER CAEA configuration is called a "double wide".)

For AER CAEA power, three electrodes are on each side of the CAEA, connected by a jumper between the inboard and outboard electrodes. Since there are two CAEAs per blade, and each CAEA needs three power wires, each blade contains six power wires. Because of this good wiring choice, the separate actuation of each elevon, and the design of the power and control system, each CAEA is independently controllable. A summary of the CAEA mass properties is given in Table 2.

Table 2. CAEA mass and c.g. properties.

CAEA (6.25in span)

Description	Dim. in	Weight lb	Arm in	Actual Weight lb
CAEA		0.273	1.944	0.2683
Actuator Fill Strip	.091 x .490 x 3.85	0.012	1.975	0.0037
HE Magnet	.125dia x .200	0.00067	5.135	0.00066
Total		0.286	1.953	

Single Wide Assy (2.875in span)

Description	Dim. in (qty)	Weight lb	X start in	X finish in	Y cg in	X cg in
LE Joiner		0.037	0.101	0.352	-0.058	0.24
Actuator & Fill	2.875 x 2.875 x .033 (2)	0.069	0.336	3.201	-0.113	1.775
Link		0.0205	3.206	4.77	-0.084	3.93
Elevon & Fairing		0.0075	4.82	5.67	0	5.19
Total		0.134				1.872

Note: X = 0.0, Y = 0.0 is at the LE on the chordline.

CAEA/Blade Integration

Each CAEA is attached to the blade with spanwise strips of a soft elastomer. Because the elastomer inhibits the motion of the elevon, only enough elastomer has been used to properly retain the CAEA. The size and distribution of the elastomer strips have been tailored for the mass properties of the CAEA, to provide a relatively uniform shear loading of the elastomer. In addition, a portion of the CF that acts on the two Lower CAT Actuators is transmitted into the blade through the flexural hinge. The adequacy of the CF load restraint system – elastomer, adherents, and flexural hinge – has been demonstrated in several tests, including bench pull tests (Ref. 16) and two (short radius) centrifugal tests (Ref. 16).

The completed AER Blades are shown in Figure 7. Each blade has two elevons (white). Power is provided to the two CAEAs via a 6-wire shielded cable, that exits the blade root

at the leading edge. The instrumentation connector is just outboard of the blade root, on the aft side. A large number of strain gages have been included in one of the blades, with the other blades having just a few gages plus dummy wires and ballast where the other gages would be. One of the blades has had a small tip weight added to satisfy the mass balance tolerance. Cross-sectional mass balance is achieved by use of segmented Tungsten leading-edge weights.

Figure 7. Fabricated blades (top view).

The lower surface of the CAEA is essentially flush with the lower surface of the blade, with the CAEA bonded in a recess in the blade structure. Thus, the lower surface airfoil profile is uniform along the entire length of the blade, except for a small gap at the elevon edges. The CAEA/blade joints are filled and faired. There are small surface irregularities near the CAEA/blade joints, elevon Hall Effects/magnets, and power wire junctions. The upper surface airfoil profile is uniform, except for elevon edges and the upper surface interface between the elevon and the main airfoil (Figure 1), which has a small gap to allow unimpeded motion of the elevon. (Flow through the gap on the leading-edge of the elevon will not occur, since the flexural hinge blocks the flow.)

The structural design of the passive section is shown in Figure 8. Note that the spar did not fill the entire blade section. Instead, foam and a light weight lower skin are used to complete the airfoil contour, with the foam removed in the active sections and the lower skin offset and bonded to the interior lower skin, thus making room for the CAEA while retaining a uniform spar. This is not the most structurally efficient approach, but it leads to relatively uniform and consistent blade properties and simplifies fabrication. Also evident in the figure are the six power wires (inside the spar at its leading edge) and the instrumentation wires (on the aft heel of the spar).


Figure 8. Design drawing of passive section.

The combined loading stress/strain of the AER CAEA is not well known, especially for the actuators and flexures. Various component tests demonstrated that the individual components could function properly under simplified loading. Proper performance of the actuator under combined loading, though, was not certain. The CAEA/blade joint was designed for an ultimate factor of safety of at least 2.0, relative to the 113% RPM centrifugal loading. The joint performed well during AER testing, properly retaining the CAEAs on the blade.

It is possible that the elevon(s) will become unstable, either through a 1-DOF (degree of freedom) flutter or some kind of aeroservoelastic coupling with the rotor blade and/or wake. This issue is exacerbated by the fact that the elevon is hinged very near its leading edge (Figure 1) without any control surface balance weight; thus, the elevon center of gravity is aft of the hinge. No elevon instability was observed during rotor testing, although an un-commanded oscillation was experienced during airfoil testing (described later).

Blade Properties

In order to support the validation of comprehensive rotor analyses, the rotor blade properties have been well controlled and characterized, and a spanwise distribution of blade strain gage bridges were installed and calibrated.
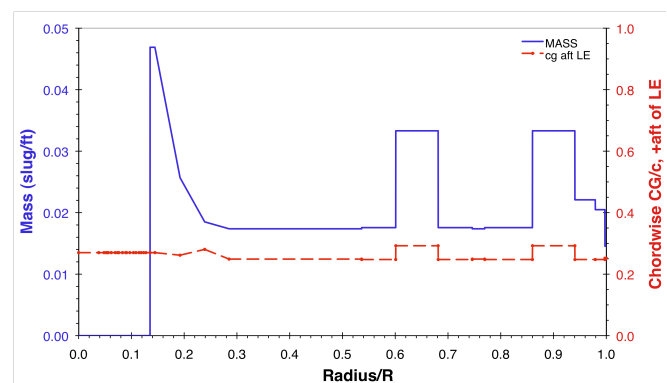
Figure 9. Radial distribution of the blade mass and chordwise center-of-gravity.

Blade section and (total) blade c.g. measurements were made on various test articles. For the Proof Blade, six (6) sections were measured, revealing c.g. locations between 0.267 and 0.270 chord (c), or up to 0.7% c aft of the design specification (of 0.263 c). Accounting for a measurement accuracy of ±0.2% c, the worst c.g. was 0.9% c aft of the design specification. An increased (full) complement of Tungsten leading-edge weights were incorporated into the Production Blades, to move the average, passive section c.g. forward, from 0.268 c to 0.249 c. This decision was informed by pre-test stability calculations, that showed strong coupling between torsion and flap modes, producing large changes in stability in the vicinity of the nominal rotor speed. Calculations also showed that moving the c.g. forward had a positive effect on blade couplings/stability. The radial distribution of the blade mass and chordwise center-of-gravity is plotted in Figure 9. Average blade

properties and blade-to-blade variations (tolerances) are listed in Table 3, relative to the design requirement.

**Table 3. Measured blade properties and variations (Tol), four production blades, after final balance.**

	Avg	Tol	Rqt
Weight			
	(g)	(---)	(---)
1 CAEA (calc. avg.)	158.6	0.75%	N/A
Blade	1983.7	0.12%	±0.50%
Center of Gravity			
	(in)	(in)	(in)
Spanwise (STA)	41.94	0.042	±0.057
Chordwise (from LE)	1.604	0.018	±0.057
First Mass Moment			
	(lb-in)	(---)	(---)
Blade	183.40	0.05%	±0.60%
Stiffness, Passive Sect.			
	(10^6 lb-in^2)	(---)	(---)
Flap	0.1031	2.92%	±5.00%
Chord	4.45	3.85%	±5.00%
Torsion	0.0456	3.59%	±5.00%
Fixed-Free Freq., Horiz.			
	(1/rev)	(---)	(---)
Flap1	0.25	0.00%	±4.00%
Chord1	1.24	3.51%	±4.00%
Flap2	1.46	1.80%	±5.00%
Torsion1	3.44	0.45%	N/A
Flap3	3.91	1.72%	N/A
Flap4	7.30	1.69%	N/A
Chord2	7.79	2.27%	N/A
Torsion2	10.26	0.20%	N/A
Elastic Axis			
	(---, in)	(---)	(---)
Elastic Axis	0.20c	0.02c	0.01c
	1.145	0.109	±0.057

Comprehensive Analysis Model

Calculations were made using the comprehensive analysis, CAMRAD II (Refs. 17 and 18), versions 4.4 thru 4.7. The model used is similar to the model defined in Ref. 11, except that the rotor and inflow models were updated and the analysis is restricted to hover. A plot of the predicted blade frequencies as a function of rotor speed is given in Figure 10.

CAMRAD II inputs were based upon measurements of the Semi-Span specimen, the Proof Blade, plus predicted changes for the Production Blades. The design and properties include the increased (full) complement of Tungsten leading-edge weights. Since the measured Production Blade property variations satisfied the design requirement, these inputs were expected to be reasonably accurate.

All calculations were performed using a common structural model. This model consisted of eleven (11) structural elements for the blade, and several rigid elements defining the articulating portions of the hub.
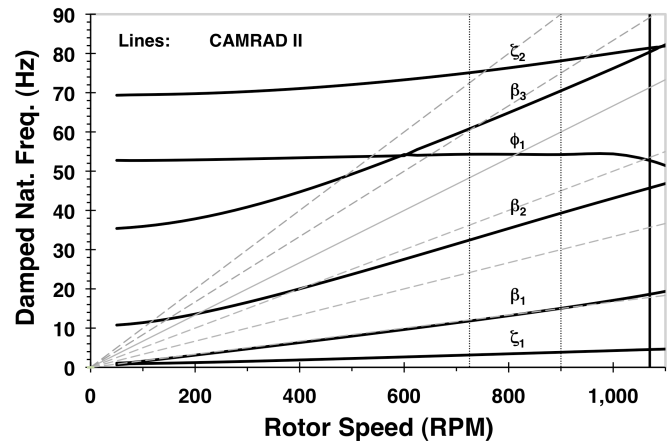
Figure 10. Variation of damped natural frequencies with rotor speed – numerical predictions.

Modal solutions were used for Flutter solutions, including modal damping of 0.5% critical for the first eight (8) modes (i.e. through about 10/rev). Flutter solutions with aircraft modes included only one (1) or six (6) blade modes. Generally four (4) aircraft modes were included in the ground resonance calculations, to include the first two modes in each of the two primary axes.

Although the lag damper uses a rubber element for the damping, the damper is modeled as a viscous damper in parallel with a linear spring stiffness. Thus, the damper model is inaccurate for dual-frequency motion.

A rigid swashplate model was used with a pitch link modeled by a linear spring element, with a stiffness of 401,000 lb/ft. The stiffness is based on analytical predictions for the pitch link stiffness and the pitch horn stiffness, combined in series.

Both a rigid fuselage and a flexible fuselage were modeled. Results were calculated for an isolated rotor (i.e. a rigid fuselage) except for the aeromechanical stability results, which include the effects of test stand flexibility by use of aircraft modes.

The aerodynamic surface of the blade was modeled as a lifting line with twenty (20) aerodynamic panels without a tip-loss correction. The blade aerodynamic loads were calculated using table look-up to account for static nonlinearities due to angle of attack and Mach number. The airfoil table was developed by Boeing for a variant of the VR-12 similar to the airfoil contour being used for the AER, with CAMRAD II adjustment for zero-lift angle and a moment coefficient increment to account for a tab angle change. Two unsteady aerodynamic models were used – incompressible thin-airfoil theory and ONERA EDLIN (Ref.

19). The former was used for blade frequency calculations; the latter was used for aeromechanical stability calculations. Dynamic stall was neglected throughout. The Uniform Inflow model was used for results presented herein.

Although not used herein, the elevon was modeled as a prescribed aerodynamic flap. Thus, no effects were included for elevon dynamics and elasticity. Linear aerodynamic coefficients of cl_δ = 2.29/rad and cm_δ = 0.427/rad were used. These aerodynamic values are believed to be a good linearized choice from the nonlinear results given in Ref. 20. CAMRAD II calculations have not included any corrections for elevon end losses due to finite-span effects.

A number of model property variations were analyzed, although they are not present herein. In particular, several models were analyzed for different blade chordwise c.g. positions, both for conservatism (aft c.g. for the whole blade or just in the active sections) and theoretical mitigation (lumped masses at the blade root and tip or in the active sections). The blade torsion stiffness, GJ, was reduced to 83% of the baseline value for some calculations. Ground resonance calculations included variations of the stand modal mass (bigger for understanding and smaller for conservatism), stand damping (reduced), and without aerodynamics (i.e. in a vacuum).

TEST STAND DESCRIPTION

Overview

The Army Rotorcraft Test Stand (ARTS) is designed to support, drive, control and measure performance of model rotors requiring up to 800 hp and generating up to 3000 lb of thrust. A hub has been developed, including analysis for a peak thrust loading of ±2000 lb and a spline torque limit of 13,750 in-lb peak. Although some individual stand components have been used in previous testing, the system as a whole and many of the subsystems were designed, implemented and tested for the first time during the course of this research program.

The system is currently powered by two 200 hp electric motors, developed by Able Corp. (now Aerophysics Research Instruments, PN 32080). The motors are installed on a combining transmission providing a 5.40:1 gear reduction. A clutch connects each motor to the input shaft of the transmission, so that a jammed motor will not impede the rotor shaft from being driven by the other motor. This also facilitates single motor operation as was the case for all of the reported hover tests.

The rotor balance is the VSB-68, that was developed by Vought Aircraft Co. (currently Triumph Aerospace). The VSB-68 is of a "concentric sleeve" type. The balance is calibrated to output three forces and two moments and can be mechanically locked by the insertion of expanding pins. The function of the balance is unusual in that the measurement elements are loaded in the axial direction (instead of bending), thus providing higher stiffness. The

flexible coupling between the stand extension shaft and the balance shaft is instrumented for torque and residual axial force. Combined, the balance and instrumented coupling provide measurement of all six rotor loads – three forces and three moments. Although the balance remained locked during the AER testing, torque measurements were acquired, and the VSB-68 represents a significant test apparatus for rotors of this size.

The swashplate assembly (Figure 11a) was developed by NASA Ames. It is composed of concentric gimbals, one for lateral and the other for longitudinal cyclic pitch, riding on top of a rise-and-fall collective. It includes three actuators that are designed to independently control collective, lateral cyclic and longitudinal cyclic pitch. The swashplate assembly is supported by the metric side of the balance.
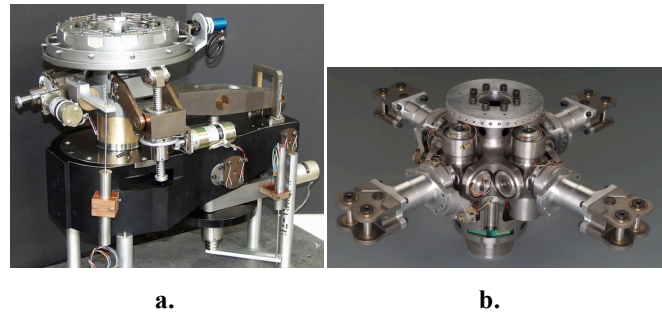

a.   b.

Figure 11. a) Swashplate and b) articulated hub.

The hub (Figure 11b) was developed by Advanced Technologies, Inc. for the AER project. It is a fully articulated, four bladed hub with coincident flap and lead-lag hinges with a 2.97 inch hinge offset. The pitch axis is further outboard and uses tension-torsion straps for CF retention, with the blade grip pins 10.53 inches from the hub center. The hub is lightly damped in lead-lag, and the stand also has low damping (Table 4), but avoidance of ground resonance can be assured by keeping the stand fundamental modes above the frequency of the rotor regressing lag mode. The hub has a large deflection range, ±9° in lead-lag, ±24° in pitch and +11 to -8° in flapping. Hub motions are measured using Hall-effect transducers.

**Table 4. ARTS (braced) modal properties (baseline).**

Mode	Freq (Hz)	Damp (% crit)	Modal M (slug)
LAT' 1	36.05	1.510	4.99
LNG' 1	39.23	1.492	2.22
LAT' 2	42.36	1.368	4.24
LNG' 2	46.11	0.744	211.05

Primary stand utilities include cooling water for the electric motors, lubricating/cooling oil for the transmission, and two oil mist systems for the balance and the stand extension-shaft bearings. The electric motors are driven by a 500-Hz motor/generator (MG) set. Stand bearing temperatures and oil pressure are monitored using a stand-alone data logging and display system.

A two-view drawing of AER/ARTS in the Hover Chamber is provided in Figure 12. Note that the rotor is within ground effect, with a height to diameter ratio of 0.78, and the rotor disk is quite large for this facility. Inflow was drawn thru baffles in the ceiling (not shown) and exhausted thru two roll-up doors (fore and aft) raised 3 ft. from the ground. This "flow control" concept handles only a portion of the downwash, such that a significant amount of the flow is likely turned by the floor and walls, only to be reingested by the rotor. Such recirculation can cause significant unsteady loading of the rotor, including harmonic, broadband, and transient loads.
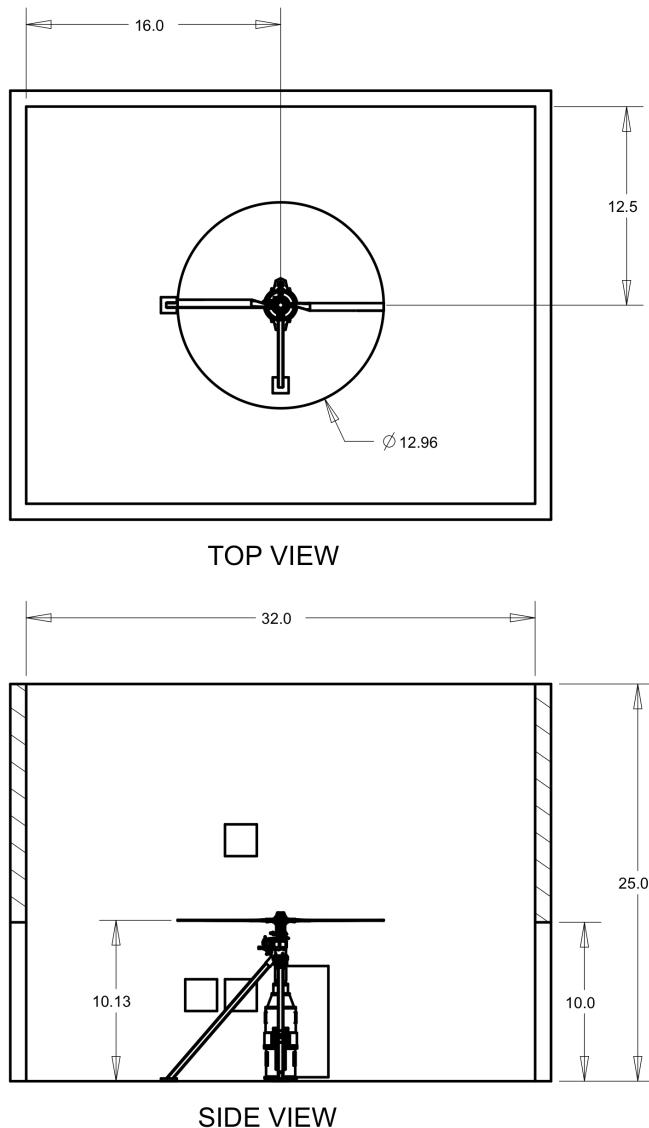
Figure 12. ARTS/AER in Hover Chamber, sketch (dimensions in feet).

Hub, Swashplate, Balance, and Design Loads

The ATI four bladed fully articulated model rotor hub is shown in Figure 11b. The hub is rated for a CF of 6,250 lb (nominal) or 7,563 lb (overspeed), and has been analyzed for ±2,000 lb thrust peak in combination with particular loads

for flap and chord bending moments, pitch link axial load, and torque (13,750 in-lb peak spline limit).

The VSB-68 swashplate assembly is shown in Figure 11a. The only external design load used in its analysis is the pitch link load – 458 lb steady, 115 lb oscillatory. These loads are both higher than those used to design the pitch links themselves.

The loads used to design and analyze the VSB-68 balance were originally presented in the form of high and low limits due to oscillatory loading but are simplified as a mean plus oscillatory. The balance positive thrust load limit is 2,500 ± 500 lb. The nominal balance side and normal limits are 800 ± 450 lb, and the pitch and roll moment limits are 9,000 ± 1,800 in-lb. The blade-out (short duration) oscillatory side and normal load limit is 7,500 lb, which is higher than that of the ARTS support. The VSB-68 torque limit is 27,600 ± 6,000 in-lb, which is higher than the strength of the articulated hub spline.

The ARTS primary structures (developed by Micro Craft, now Triumph Aerospace Systems) and drive system (developed by Anderson Precision Gears, NASA Ames, and Seattle Gearworks) were generally designed to the VSB-68 nominal limits, except that the torque was higher, with a limit of 58,822 in-lb peak. For a blade-out condition, the primary structure was designed to a slightly lower value – 7,320 lb for the blade-out radial oscillatory load.
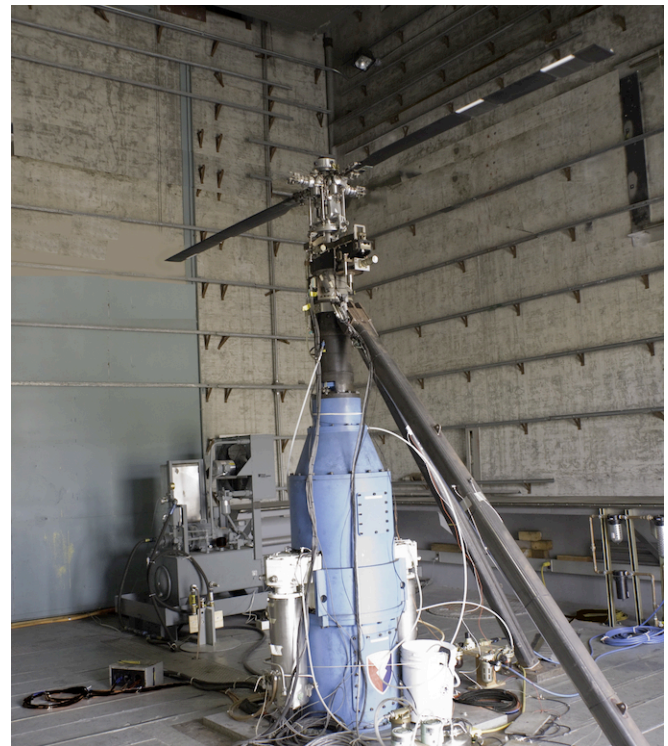
Figure 13. ARTS/AER in Hover Chamber, photo.

POWER SYSTEM DESCRIPTION

Each CAEA is driven by a power circuit (Figure 14), which contains one Power Amplifier and two DC Power Supplies. Internal to each CAEA are four CAT (Conformal Actuator Technology) Actuators, electrically combined to present three leads to the power supply circuit. The two Upper CATs act in opposition to the two Lower CATs (Figure 14), thus deflecting the elevon (Figure 1). The DC Power Supplies provide an electrical bias so that each actuator is supplied with the appropriate positive and negative peak voltages. Dynamic (largely oscillatory) voltages are provided by the Power Amplifier. Input commands can be provided to the Power Amplifier from a variety of sources, including function generators and DECS (Dual-Elevon Control System). The DC Power Supplies are Lambda Genesys™ Gen 600-2.6, a programmable switching power supply. The amplifiers are Rohrer HERO® Precision Power Amplifier PA9812A, a linear regulated, four quadrant, precision power amplifier. A capacitor box was developed and used to test the power system.
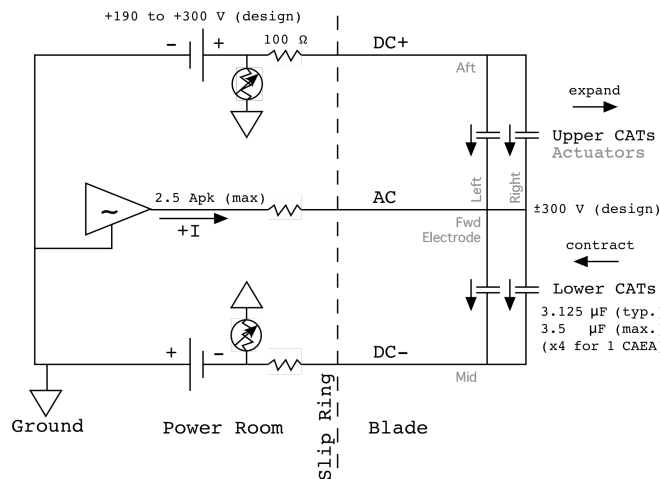
Figure 14. CAEA power circuit.

Because the DC Power Supplies could not sink current, a custom switched resistor bank was developed. Depending on the DC voltage level being used, the switch was set to the appropriate setting, and sufficient current was dumped to ground to allow the needed oscillatory current thru the HERO®s and CATs while not requiring any current to be absorbed by the power supplies. The circuit design requirements are noted in Figure 14, although some components were designed to operate at higher currents. The Power Amplifier has a maximum current output of 1.77 Arms (2.5 A peak).

CONTROLS DEVELOPMENT

The objective of each control algorithm was to provide elevon position control. The first step in the design process is the development of models of the actuator assemblies (CAEAs or "elevons" in this section), as described below.

Plant Model Development

Since actuator bench test data exhibited a significant amount of hysteresis that varied with frequency, initial model development included Preisach concepts as well as some new formulations. Due to time and complexity, those models were abandoned in favor of a quickly identifiable, linear transfer function representation, which would provide an accurate linear plant model but neglect nonlinearities such as hysteresis and material saturation. The effect of hysteresis was then dealt with by increasing the phase margin requirements of the system.
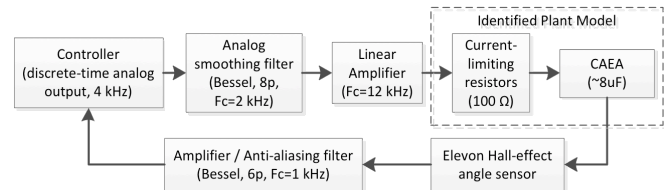

Figure 15. Control system block diagram.

The block diagram depicted in Figure 15 shows which parts of the system were interconnected and which needed to be identified. The dashed rectangle portion consisting of the resistors combined with the actuator assemblies was the portion of the signal chain that needed identification.

In order to develop linear models of the AER elevons (CAEAs, paired with resistors), input voltage frequency sweeps were conducted on the elevons as mounted on the blades and rotating in the hover chamber. Frequency sweeps were conducted for all elevons, at the control design rotor speeds (0, 725, and 900 RPM) with 2 deg collective pitch; raw elevon angle data were collected. The nominal frequency range of the sweeps was from 20-275 Hz (125-1728 rps, radians/second).

The input (voltage) and output (elevon angle) data pairs collected during the frequency sweeps were then processed through the Comprehensive Identification from Frequency Responses (CIFER®) tool, developed at AFDD (Ref. 21). Non-parametric input to output frequency response models were generated for all the elevons at all control design RPM settings. It was noted that the dynamic responses of the elevons are dominated by a very lightly damped primary resonance around 1200-1500 rps (190-240 Hz). The frequency and damping of this mode varies among the elevons and also as a function of rotor speed. For example, Figure 16 depicts the change in response magnitude and phase with rotor speed for IBB1. Note that at 0 RPM the response shows the least amount of damping of the resonant mode. This is to be expected since when the blades are rotating aerodynamic damping adds to the natural damping of the elevon motion. There also seems to be a slight increase in the natural frequency with increasing RPM. Finally, the steady state response is reduced with increasing RPM. Both of these last two effects (frequency and steady state response trends) were anticipated due to the increasing

dynamic pressure and associated "aerodynamic spring stiffness" with increasing RPM.
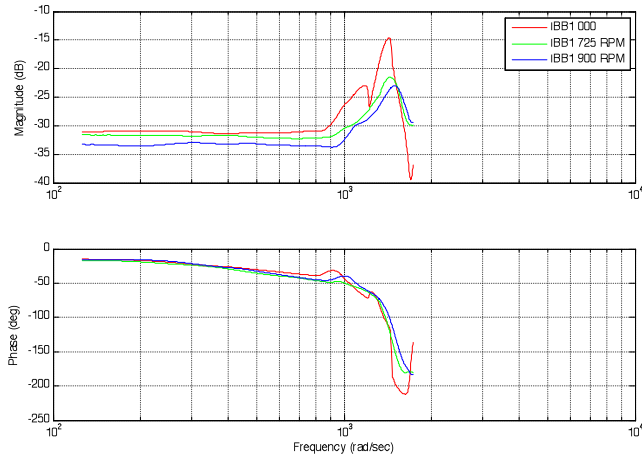
Figure 16. Typical variation of elevon response to rotor speed.

The non-parametric models were then fit with transfer functions using CIFER®'s NAVFIT facility. $2^{nd}/3^{rd}$-order transfer functions were used, such as in the equation below.

$$\frac{-6.17s^2 + 18158s + 26789264}{s^3 + 719.1s^2 + 2238840s + 945079104}$$

Similar plant models were created for each available elevon and rotor speed combination for use in the control design and optimization process and to ensure robustness. All elevons behaved in a roughly similar manner, but they were different enough to make control design challenging. Table 5 summarizes the characteristics of the second order resonances fit to each of the elevons at various RPMs using CIFER®.

Table 5. First resonant mode of various elevons.

	On Blade, 0 RPM		On Blade, 725 RPM		On Blade, 900 RPM	
	Freq (rps)	Damp	Freq (rps)	Damp	Freq (rps)	Damp
IBB1	1380	0.0531	1460	0.0937	1510	0.101
IBB3	1460	0.0457	1340	0.0753	1380	0.0841
OBB1	1190	0.0348	1240	0.0674	N/A	N/A
OBB3	1290	0.028	1530	0.0928	N/A	N/A

The experimental datasets were also processed using the MATLAB Identification Toolbox, which produced very similar linear parametric models as well as goodness of fit metrics.

Control Design Goals and Constraints

The controllers were designed to provide elevon position control. The controller performance requirements were stated in terms of control bandwidth and disturbance rejection capabilities. The definition of control bandwidth adopted was the ability to provide close to unity response-to-

command ratios across a wide frequency range. The control bandwidth was defined as the maximum frequency below which response-to-command attenuation is less than -3 dB, with the provision that everywhere else in that frequency range the ratio never exceeds +1 dB. Note that this is strictly a magnitude measure. The associated measure of response-to-command phase accuracy is the phase lag metric (typically -45°), but that was not looked at here. The measure of disturbance rejection performance used was Disturbance Rejection Bandwidth (DRB) as defined in the Test Guide for ADS-33 (Ref. 22). DRB is the highest frequency on the disturbance response curve for which the disturbance response is below -3 dB.

The design goal was to achieve the highest control and disturbance rejection bandwidths possible, with a target frequency of 5/rev (i.e. 89 Hz or 560 rps at a rotor speed of 1070 RPM or 17.83 Hz). From the outset it was understood that achieving these goals would be difficult, given the very lightly damped primary resonant mode of the elevons. For systems with similar resonant modes, generally structural, it is well known that achieving crossover frequencies higher than about 1/5 to 1/3 of the resonant frequency would be difficult while maintaining good stability margins (Ref. 21).

For the range of resonance frequencies noted earlier for the elevons, this meant that a crossover frequency range of 240-300 rps would be expected. Of course, given that the same exact controller would be used on all the elevons, only the lower value of 240 rps would be applicable. Additionally, care had to be taken with the aggressiveness of the controller so as not to exceed certain rate limits which are related to current limits of these electrically actuated devices.

Higher crossover frequencies, and therefore better performance in terms of bandwidth and disturbance rejection, would be more easily attained if the damping of the resonant mode of the elevons could be increased. This may be possible either through improving the mechanical damping of the elevons in production or through feeding back elevon-angle-rates in the controller. The elevon-angle-rates for the latter option would either come from measurements or be calculated by differentiating the elevon angle data. There is no currently available sensor for measuring the elevon-angle-rates, therefore, differentiating the elevon angle measurements would be the only viable option. Since the resulting rate signal would be of very low quality due to noise, elevon-angle-rate feedback is not an attractive option. Therefore, the preferred path towards better system performance would be increasing the mechanical damping of the elevons (CAEAs).

Two different controllers were developed for closed-loop control of the elevons. The controllers were developed independently and following two completely different design approaches, one classical and another Model Predictive Control (MPC). The classical controller was developed first as a preliminary means of achieving as much

of the closed-loop elevon performance requirements as possible while the more sophisticated MPC controller was being developed. The same set of performance requirements, stated earlier, was used for both controllers. Interestingly, as will be shown later in this paper, the two highly dissimilar controllers displayed very similar overall final performance, both in analysis and in actual hover chamber tests.

Figure 17 shows a typical Simulink® block diagram model of the system used to design the controllers. In this way, various controllers, smoothing filters, identified plants, disturbance inputs, anti-aliasing filters and observers could be tried in combinations in an automated way to help with robustness and decrease the labor of creating new models.
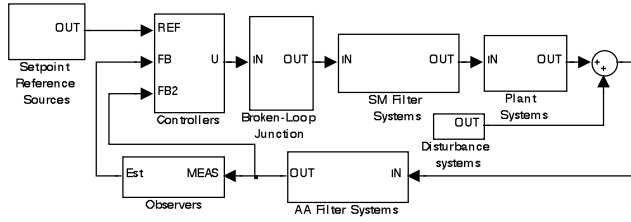
Figure 17. Control system block diagram used in simulation.

Classical Controller

A simple classical controller was designed as a preliminary means of achieving as much of the closed-loop elevon performance requirements as possible while a more sophisticated controller was being developed. The simple controller employed unity feedback of only the elevon angle (with a time delay representation of the anti-aliasing filter). No rate measurements were available or reconstructed for control use. The forward path consisted of an integrator followed by a lead/lag network and a notch filter placed roughly at the location of the primary resonance mode of the elevons. A time delay representation of the hardware smoothing filter was also placed in the forward path. Figure 18 shows the Simulink® block diagram representing the controller portion.
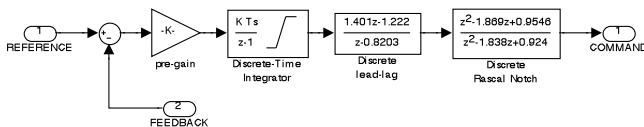
Figure 18. Classical controller block diagram.

The notch filter was implemented as a $2^{nd}/2^{nd}$ transfer function. This implementation essentially placed the frequencies of the second order poles and zeros at exactly the same location. A lower damping ratio for the second order zeros (relative to the second order poles) was then used to achieve the magnitude notch with little effect on the phase response. The lead-lag network was implemented as a first order zero over a first order pole, with the steady state gain normalized to unity. The motivation toward use of the lead-lag network was to improve gain margin by adding lead

(additional phase) in the region of crossover. Control analysis and optimization were carried out using the Control Designer's Unified Interface (CONDUIT®) tool developed by AFDD (Ref. 23).

Within CONDUIT®, optimization proceeds in 3 consecutive phases, first ensuring stability and satisfactory margins, then achieving required performance, and finally ensuring that the system is not overdesigned. To ensure robustness to variations in the characteristics of the elevons, discussed previously, all available elevon models were included in the first phase of the optimization to ensure stability, acceptable margins (a phase margin of 45 degrees and a gain margin of 6 dB), and good damping. For the 2nd and 3rd phases of optimization, however, the 0 RPM models were not included as elevon performance while stationary was not of concern – only stability.

MPC Controller Background

The advanced architecture explored was Model-Predictive Control (MPC), a member of the optimal class of controllers. In brief, MPC makes explicit use of the plant model in its formulation to simultaneously optimize a finite number of control steps (N_c steps) through a finite number of prediction steps (N_p steps), only implementing the next move. This is repeated at each control cycle. Since the controller has an explicit approximation of the model, it can attenuate the command near the resonant frequency and optimize for the system delays through explicit prediction and functional cost minimization; the selected cost function was

$$J = (R_s-Y)^T(R_s-Y) + \Delta U^T R_w(\Delta U) \qquad (1)$$

where

$$Y=Fx+(\Phi)\Delta U \qquad (2)$$

is the output over the prediction horizon, which yields the following control law:

$$\Delta U = (\Phi^T\Phi+R_w)^{-1} \Phi^T(R_s-F x) \qquad (3)$$

where

$$\Phi = \begin{bmatrix} CB & 0 & 0 & \cdots & 0, \\ CAB & CB & 0 & \cdots & 0 \\ CA^2B & CAB & CB & \cdots & 0 \\ \vdots & \vdots & \vdots & \ddots & \vdots \\ CA^{N_p-1}B & CA^{N_p-2}B & CA^{N_p-3}B & \cdots & CA^{N_p-N_c}B \end{bmatrix} (N_p \; x \; N_c)$$

Figure 19. The Toeplitz matrix of the system.

The Φ matrix (Figure 19) can be thought of as the necessary transform to predict the portion of the output due to a change in command (ΔU). Φ has dimension (N_p x N_c). The F matrix (shown in Figure 20) has as many columns as outputs, but is only a vector in this situation since this is a single-output system. F can be thought of as the necessary

transform to predict the portion of the output due to the current state of the system and its evolution; it has dimension N_p. R_s is the vector of future reference setpoints around which the optimization will be performed.

$$F = \begin{bmatrix} CA \\ CA^2 \\ CA^3 \\ \vdots \\ CA^{N_p} \end{bmatrix} \quad Rs = \left.\begin{bmatrix} r_{k-N_c} \\ r_{k-N_c+1} \\ \vdots \\ r_{k-N_c+N_c} \\ \vdots \\ r_{k-N_c+N_c} \end{bmatrix}\right\} N_p$$

$$R_w = \begin{bmatrix} w_k & w_{k+1} & \cdots & w_{k+N_c-1} \end{bmatrix} I$$
$$x \equiv augmented\ state\ vector$$
$$(A, B\ and\ C\ are\ state-space\ matrices)$$
$$(r_i's\ are\ future\ reference\ targets)$$
$$(w_i's\ are\ the\ future\ step\ weights)$$

Figure 20. The Hankel matrix and other MPC-related equations.

Note that in this formulation, the actual command "U" is not referenced; instead "ΔU" is used. Because of this, the controller is actually optimizing the relative states in the system. This is true for all states except the augmented state, described next. An important aspect of MPC is its need for explicit, expected behavior in the plant, including the contributions of noise and disturbance. To this end, the system matrix was augmented to include a single integrator that ensures zero offset for a constant set point and slightly improved disturbance rejection bandwidth (DRB). If the model that is embedded into the controller is not accurate enough, the performance of the controller suffers severely due to the assumptions made about the state evolutions, etc. The general approach with MPC is that the expected performance of the controller is directly related to the accuracy of the model, since it can take an arbitrary number of effects into account (even non-linear and boundary conditions), but as in all control designs, the internal model was as accurate as practically possible for this project. The model need not be perfect, since we are only implementing the first move of the optimization, but the more accurate the model, the better the optimization will be; the better the optimization is, the better controller performance that can be achieved.

This formulation is based heavily on the first controller example in Ref. 24, but has been modified in some areas to be better optimized for this application.

MPC-specific Model Development

The $2^{nd}/3^{rd}$-order elevon assembly model was combined with linear models of the surrounding electronic components (smoothing filter ahead and anti-aliasing filter following) to yield a high-order system model. In Figure 15, the component blocks are shown; transfer function models of each were found, finally producing an 8th order model for the smoothing filter and a 3rd order model for the anti-aliasing filter.

This high-order, continuous model was constructed by connecting the component models in series yielding a $8+3+3=14^{th}$ order model. This was then converted to a discrete, lower-order system by first using a MATLAB built-in function which converted from continuous time to discrete time (4 kHz). Next the model order was reduced using another built-in function which takes a higher-order model, analyzes the energy in the states and provides a "balanced" reduction of the order in such a way as to salvage as much of the dynamic state energy contributions as possible. This reduction was done to minimize the computational burden of evaluation so that the controller could be executed in real-time. The reduced-order, discrete state-space model maintained the vast majority of its state energy at 5th order. One extra state was added to this total for disturbance rejection and steady-state error elimination. As mentioned, MPC needs to have an explicit notion of the goals it will accomplish and the model it is controlling. Since the states are formulated in a relative way ("ΔU"), this extra state integrates feedback of the difference between the reference setpoint and the actual feedback. This extra state was placed into the model as shown in Figure 21, which gave us a final 6th order model. This is one of the simplest disturbance models that can be used in MPC and was implemented due to simplicity.

$$A = \begin{bmatrix} A_m & 0_m^T \\ C_m A_m & 1 \end{bmatrix} \quad B = \begin{bmatrix} B_m \\ C_m B_m \end{bmatrix} \quad \begin{array}{l} C = \begin{bmatrix} 0_m & 1 \end{bmatrix} \\ Matrix_m \equiv \\ pre-augmentation \end{array}$$

Figure 21. MPC internal model augmentation.

MPC Implementation

An important aspect of the overall system design was the need to keep input and output parameters within tight limits for the safety of the elevon assemblies and the rotor while balancing the control authority of the controller. While it is possible to implement this in an MPC controller, the decision was made to not take any of these boundary conditions into account, thus maintaining the controller's linearity and allowing the associated analyses for stability, disturbance rejection, etc. but leaving the detection and correction of those boundary conditions to other subsystems outside the controller proper or to the human operator. This tradeoff was made not only to keep the controller linear (making those analyses discussed above possible), but also for the sake of computational efficiency, since a non-linear MPC controller must take an iterative approach to the solution at each time-step instead of the single computation possible with the linear version.

The final MPC controller was selected to have a prediction horizon of 15 steps and control horizon of 5 steps. The number of control steps was selected to allow a stable control horizon since the rise-time of the model was approximately 4 control cycles long (1 ms). The prediction horizon of 15 steps was selected to allow the model to settle and stabilize after the control moves were implemented. These decisions were partially informed from Ref. 25.

Since this MPC formulation depends on the internal states of the model (the 6th order, MPC-specific model discussed above), but only one variable was being measured

(the elevon angle), there was a need to estimate the 5 states that were unknown.
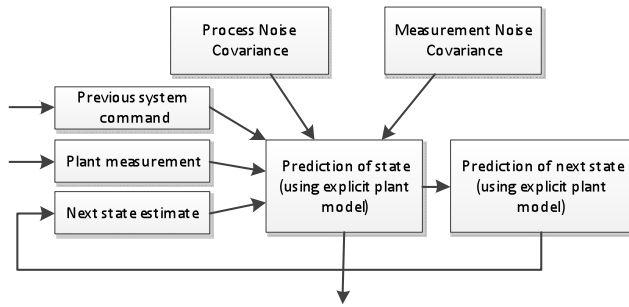

Figure 22. Kalman Filter Algorithm.

The state observer (a Kalman Filter) was tuned by adjusting the process noise covariance and measurement noise covariance matrices along their diagonals, assuming no cross-state covariance. The lower limit for the process noise covariance estimates were determined numerically by searching for the values that resulted in instability of the observer while using realistic noise estimates to taint the simulated sensor feedback while executing frequency sweeps with the full, identified plant model within Simulink®. These coefficients (all 5 equal in this case) were then increased until the closed-loop response became noticeably degraded. The value just before noticeable degradation was then used.

The measurement noise covariance selection was based on experiments with the sensors and filters, allowing the Kalman filter slightly higher values as this design needed to maintain a conservative, robust state estimator which would not be susceptible to instability in the face of slight measurement noise increases.

Once the state observer was tuned, the design effort to tune the controller step weights consisted of a manual process of adjusting and observing stability margins as well as command and rate limits while trying to optimize toward the goal of increasing DRB and closed-loop bandwidth. Gain and phase margins of at least 6 dB/45 degrees were maintained, with DRB peak response of no more than 4.5 dB.
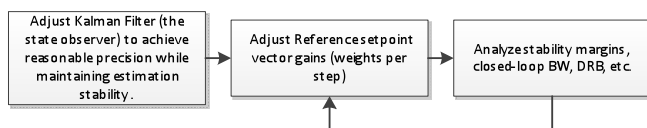
Figure 23. MPC tuning algorithm.

Before the estimator was included in the design, full state feedback from the model was used from the simulation model; this is a typical design approach for architectures that need state observers so as to understand whether the controller has good potential for success. In this synthetic condition, the stability margins and closed-loop bandwidth demonstrated by the controller were considerably higher

than in the final design (all associated design goals were satisfied). There were still issues with the disturbance rejection peak response, however. Once the estimator dynamics were included, closed-loop bandwidth and stability margins decreased, but the design was still limited by disturbance rejection peak response. This gives hope for the future that once the higher precision estimation and improved disturbance rejection issues have been addressed, this architecture may have increased usefulness in this application.

The fixed weights (cost per control step) adjusted in the controller were at first tuned equally per-step, but it was finally found that an exponentially increasing weighting per-step, which assigned more cost to the final control moves, would yield higher stability margins and better DRB. This can be thought of as prioritizing the final positional accuracy of the optimization solution (giving it higher cost penalty) so that deviations at the end of the prediction were much closer to the reference than the beginning moves.

Many MPC implementations are not aware of future reference values (future setpoints), but in this case, the reference setpoints were pre-programmed and their futures were known. Since the delay incurred for pre-loading the reference vector was small (1.25 ms, 5 control moves), this was done and the reference vector was loaded with 5 future moves, having the 6th-15th moves equal to the 5th move, essentially creating a more realistic optimization problem for the algorithm. This approach was especially helpful to maintain stability at higher frequencies because the algorithm was aware of the future oscillations and could take them into account.

System Implementation

The coding implementation was accomplished very conveniently using xPC Target (a MATLAB/Simulink® add-in). This approach enabled a quick copy-paste workflow – from the analyzed Simulink® models to the final model – by eliminating manual translation steps. The compiled model ran on a real-time target machine operating at a control frequency of 4 kHz.

ACTUATOR AND CAEA TESTING

Domzalski Machine Tests. Significant component and assembly tests were performed by Domzalski Machine during the Phase I, II, and II+ SBIR contracts. Since only a portion of these results have been published (Ref. 15), additional details will be documented herein.

Developmental testing included material coupons, electrodes, actuators, and assemblies. Significant tests were performed to quantify actuator performance, component strengths, and CAEA performance. CAEA tests were separately performed on a bench, under rotation, and on a wing section in a wind tunnel. One successful CAEA electrical fatigue test was conducted. Select results will be described below.

As is well known, PZT exhibits a variety of nonlinearities. One significant nonlinearity is caused by saturation of the electric field levels in the PZT grains. The result is a loss of actuator effectiveness. Figure 24 provides an example, from a test of a CAT actuator prototype, with PZT sheet thicknesses of 0.011 inch. The figure is a plot of peak-to-peak values – strain versus the voltage (and electric field). Note that the slope decreases as the electric field is increased. The accompanying recommendation (July 2000) was to operate at 120 Vpp/mil, or ±60 V/mil, for which the oscillatory strain was ±690 με. Later testing of a variety of specimens revealed that operation at such high electric fields produced low reliability/life.
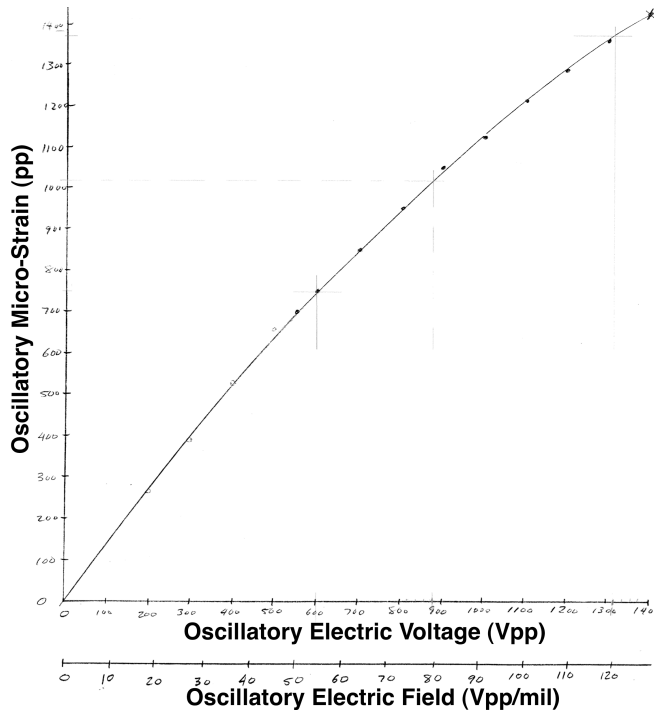
Figure 24. Effect of oscillatory electric field on CAT strain, prototype, VDC ≅ 28% VAC.

The effect of the DC voltage on actuator strain and current is shown in Figure 25. This shows that larger oscillatory strains can be obtained for lower DC bias voltage, but this comes at the expense of increased electric current. The larger strains also correspond to more extensive domain switching and lead to lower reliability/life for the actuators.

During the SBIR a variety of CAT actuator designs were developed. Figure 26 shows the measured performance for single-wide actuator designs, for AER geometries at ±300 V (generally at 6 to 10 Hz). The selected design is the pink curve with square symbols, which satisfies the design requirement.
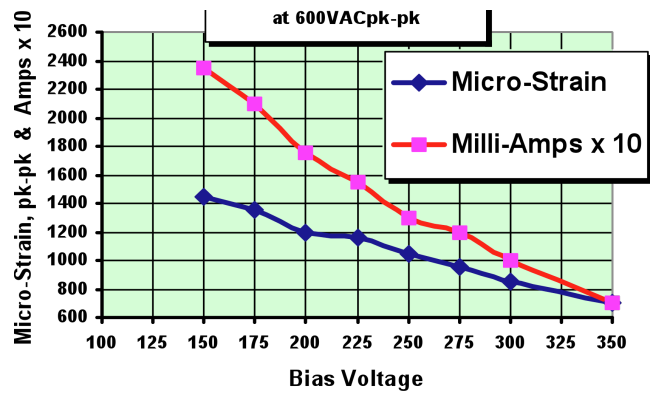
Figure 25. CAT actuator strain and current for various DC voltages.
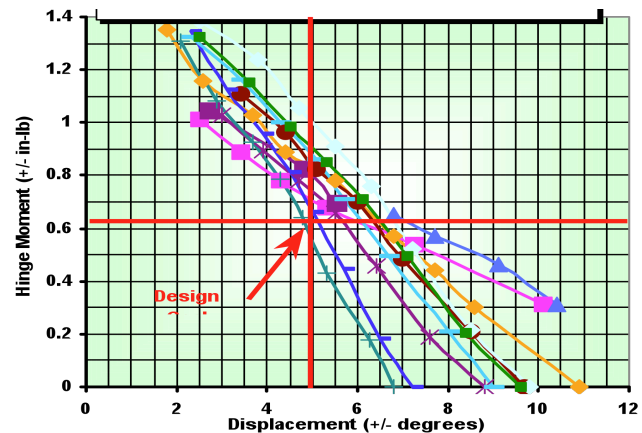
Figure 26. Actuator-elevon assembly static performance, baseline and developmental models (Ref. 15).

A 2D wind tunnel test was conducted on an active wing containing the CAEA. This test was intended to demonstrate safe operation over a range of Mach numbers and angles of attack (AOA or α), and to quantify the ability of the CAEA to meet the elevon deflection requirements. The test was conducted in the Ohio State Transonic 6 x 22 inch blow-down facility. Testing was performed with an applied voltage of 200±300 V at 10 Hz. Testing included select Mach numbers between M=0.3 and M=0.87, for a relatively small number of angles of attack generally between α=0° and mild stall, with M=0.3 including α=-2° to +16°. The airfoil was made of solid aluminum with an offset in the lower surface for the CAEA. The wing has the AER chord (5.67 inch) and a 6.0 inch span, including a full-span actuated elevon. The only measurements were of the elevon angle, wake deficit, and test section conditions.

A significant result from the test is presented in Figure 27. This figure shows CAEA performance and some uncommanded elevon oscillations (discussed later). The performance results were generally satisfactory. The nominal stiffness model achieved the required ±5° elevon deflection at M=0.56 for α=0°, with a decreasing deflection for increasing Mach number. The deflection was somewhat larger for α=3°, and significantly lower for a model with an increased stiffness for the elevon flexure. Largely based on

this figure, the nominal stiffness flexure was selected for AER.

Some limited flutter data was obtained during a 2-D airfoil test of the CAEA (Ref. 15 in part and Ref. 16). Ref. 16 included the graph shown in Figure 27, and an accompanying description of the results:

> The following graph shows how the [oscillatory elevon] deflection amplitude drops with increasing Mach until an un-commanded oscillation component becomes present giving an apparent rise in deflection amplitude at the highest Mach. The oscillation is noted here as containing the electrically driven frequency of 10 Hz and a higher frequency. The higher frequency is estimated to be around 40-50 Hz with a random amplitude. Both models sustained operation under these conditions without damage. The behavior did not change while these conditions were applied, i.e. the behavior was stable.
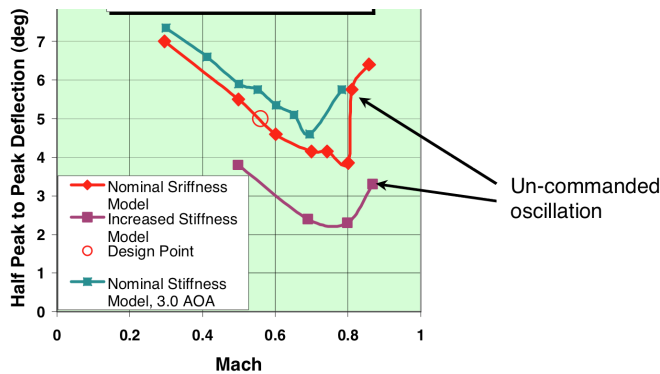
Figure 27. CAEA performance as an active airfoil in a wind tunnel.

Based on Figure 27 and the accompanying explanation, it appears that the model experienced a 1-DOF elevon flutter, starting at $M \cong 0.82$ (nominal stiffness, $\alpha=0°$) or $M \cong 0.75$ (nominal stiffness, $\alpha=3°$). For the midspan of the outboard elevon, $M=0.59$ at Ω_0, and $M=0.64$ at 110% Ω_0. Thus, at low angles of attack, even for 110% Ω_0, there is likely a 16% Mach number margin before 1-DOF elevon flutter is reached. Note, however, that uncommanded oscillations also occurred at $M=0.6/\alpha=9°$ (increased stiffness) and $M=0.68/\alpha=6°$ (nominal stiffness). Since, for these two Mach numbers, the next lowest α is 3°, the onset speed is not well defined. This phenomenon was not observed for $M=0.78/\alpha=3°$ (nominal stiffness).

The CAEA's unloaded first natural frequency was 210 Hz, but the flutter frequency was found to be much lower. In particular, the flutter frequency is 40-50 Hz (Ref. 16), which corresponds to 2.2 to 2.8/rev at Ω_0. Thus, there is potential for interaction with blade aeroelasticity, especially modes β_2 and ϕ_1.

DLR Static Airfoil Test. A static airfoil test was led by Dr. Wolfgang Geissler of the German Aerospace Center (DLR), Ref. 26. Aerodynamic loads testing was performed at ambient temperatures at the DLR Kryogenic Ludwieg Tube (KRG), that has a 0.35 x 0.4 meter test section. Instrumentation included 63 pressure tabs and a wake rake with 59 pitot tubes. Angle of attack sweeps were performed at four Mach numbers, for a baseline airfoil and static elevon deflections of ±5° (M=0.5 and 0.6) or ±3° (M=0.7 and 0.75), for a total of twelve polars. Note that the airfoil coordinates differ somewhat from those used for AER and there is limited access to the electronic test data. One value of this test is that it provides aerodynamic pressures, for potential use during future code validation.

AFDD Tests. After the AER production blades were fabricated, a separate batch of CAT actuators (see e.g. Figure 3) were procured for bench testing at AFDD. These tests were intended to qualify the electrical system for operation with the CATs, to verify the electrical rating of the actuators (190 ± 300 V), to determine if even higher electrical excitation were feasible, and possibly to allow some limited fatigue testing (not pursued).

Testing revealed a number of issues. In particular, a number of CATs exhibited premature electrical failure. Some of these failures were believed to be caused by the (2-4 kHz) digital output of the DECS. Consequently, analog smoothing filters (Fc = 2 kHz) were added between DECS and the HEROs. Additional failures were believed to be caused by a relatively aggressive hysteresis identification technique, that used a targeted progression of triangle waves with constant slew-rates. Unfortunately the higher frequency harmonic content proved to be very hard on the actuators. Consequently, a lower bandwidth technique was implemented, based on sinusoidal excitation. Continued testing produced additional failures, which led to a reduction of the oscillatory voltage limit from ±300 V, first to ±250 V, and then to ±200 V. Due to this experience with CAT reliability, and some reliability concerns described by the developer, initial hover testing was conducted with an oscillatory voltage limit of ±200 V.

After the issues with the previous CAT tests had been corrected, tests were performed on three additional CATs. These tests revealed some interesting trends with regards to strain response to voltage and frequency. Figure 28 shows data from one of the CAT specimens at 2 and 89 Hz, for a range of voltage levels. This CAT produces ±580 µε at ±250 V (2 Hz), similar to the performance shown for the CAT prototype (Figure 24). Both plots reflect material saturation effects (lower slopes) at higher voltages and relatively small hysteresis. Another specimen that was tested, though, showed significantly larger hysteresis at 89 Hz. This variability among specimens, along with schedule pressures, led to a decision to stop actuator testing in favor of assembly testing.
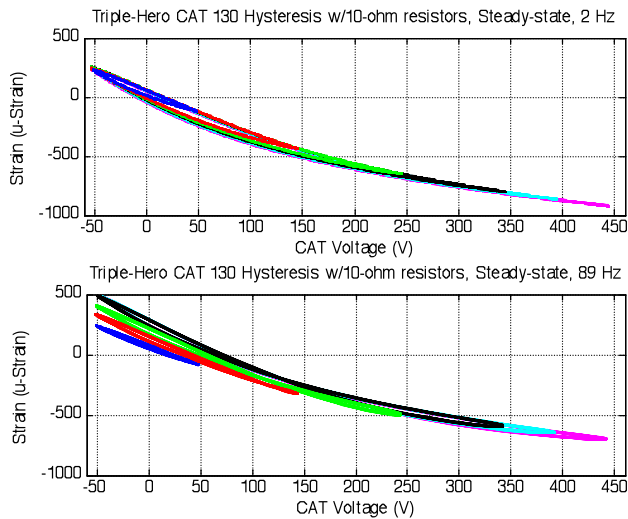
Figure 28. Low and high frequency input/output characteristics of CAT 130.

A CAEA bench test article (Figure 29) was developed to experimentally determine the hysteresis of a CAEA assembly and facilitate testing at high voltage levels against a load. The test article incorporated five linear springs along the length of the elevon, bonded to pads on either end, which were in turn bonded to the elevon and a bar that was screwed to an aluminum fixture. These five springs were ultimately reduced to 3 in order to compensate for lower-than expected actuator performance. The aluminum fixture (from the developer) also held the actuator assemblies, sandwiched between the two opposite pieces and separated from the aluminum by strips of elastomer, similar to the blade mounting. Evident in Figure 29 are a few springs restraining the trailing edge of the elevon, the two layers of the composite link, and in between, a necked down region that is the flexure, about which the actuation loads are transmitted and the elevon deflection occurs.
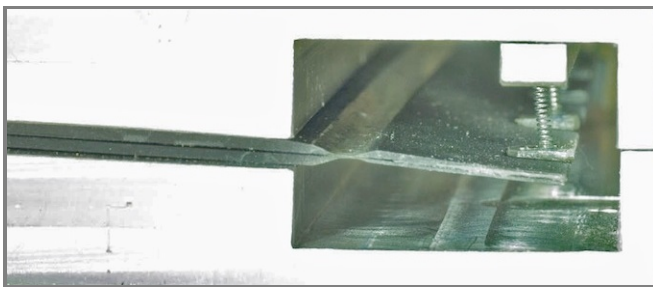
Figure 29. CAEA Bench Test Article.

Testing with this article demonstrated several useful characteristics about the assembly. Firstly, while some of the tested CATs exhibited a moderate amount of hysteresis, this CAEA demonstrated relatively small hysteretic widths. Secondly, higher frequency sweep experiments revealed the magnitude and frequency of the first resonant mode. An example time history of elevon deflection is given in Figure 30. The command for this data record included incremental changes to the DC voltage, with a sweep of the oscillatory voltage from 10 to 1000 Hz at each DC voltage level. This

scheme was developed to allow identification of hysteresis over a wide range of operating conditions, and was called a "Sinusoidal Hysteresis Identification" (SHID) algorithm. Most evident from the figure is that the resonant elevon deflection responds strongly over the full DC voltage range, and the peak-to-peak response is not a strong function of the DC voltage. This data set and others were acquired to support the development of a physics based model of the actuation system, and may also be useful to quantify the extent to which the system deviates from a linear plant model. The observed hysteresis and CAEA dynamics suggested that a linear model might suffice for the CAEAs on the production blades. Furthermore, the unexpected reduced performance of the CAEA Bench Test Article, along with schedule pressures, led to a decision to stop bench testing in favor of work with the CAEAs on the production blades. Testing of the CATs and bench test article were also valuable because it allowed refinement of the power system, data and control system, operational limits, and operating procedures.
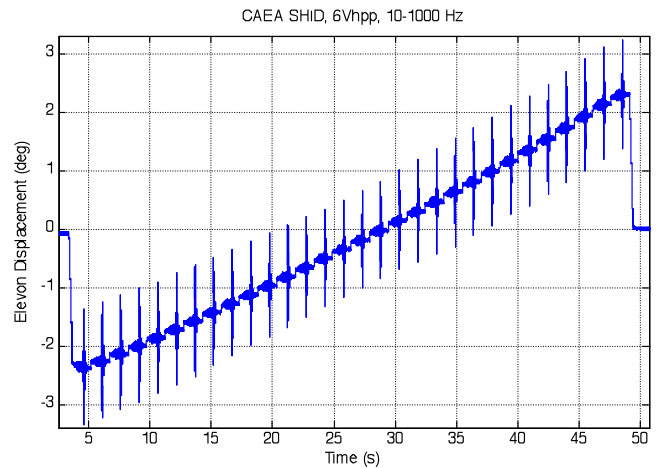
Figure 30. Elevon time history from the SHID algorithm, CAEA Bench Test Article.
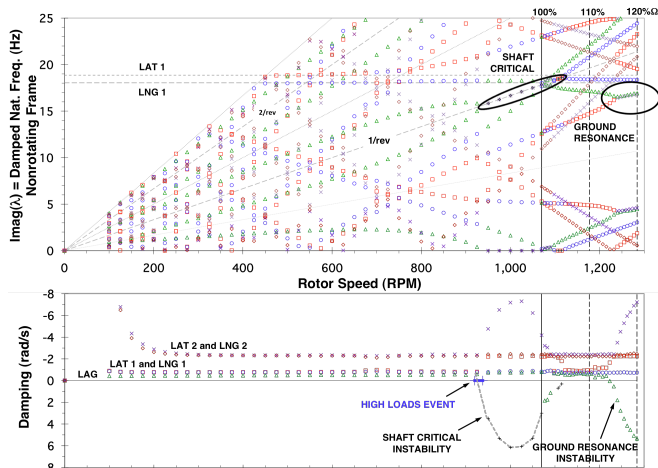
AEROMECHANICAL STABILITY

Initial rotor testing was performed with only two blades. Unfortunately, no numerical assessment was made of the aeromechanical stability of either the two- or four-bladed AER. Due to inadequate study, a dangerous instability was encountered. This was a particular problem since AER/ARTS – as originally configured – had relatively low fundamental stand frequencies of 18.4 Hz (longitudinal) and 19.1 Hz (lateral), small stand damping, and small rotor lead-lag damping (only significant for ground resonance).

During rotor speed expansion, while heading towards 940 RPM, a rotor speed was reached that caused a significant increase in the stand loads. A quick action to reduce the rotor speed did not immediately alleviate the high loads, but the rotor and test stand did remain intact as the rotor speed coasted towards 0 RPM. Analysis of the safety of flight data showed that the test stand had experienced high 1/rev acceleration, and the two blades had experienced

significant steady lag angles, in opposite directions (one leading, the other lagging). These are classic signs of a shaft critical instability, that is well explained in Ref. 27. Fortunately, post event loads review showed that the blades did not experience high loads, and the test stand loads did not harm the rotor balance (which was locked), although some stand bolts were replaced.

Aeromechanical stability calculations were performed after the event, primarily to confirm the hypothesis by correlation of the onset of frequency coalescence/instability from a shaft critical instability, and also to check for ground resonance (Figure 31). The plot shows the damped natural frequencies (in the nonrotating frame) and the damping, both as a function of rotor speed. The region of shaft critical instability is circled on the frequency diagram, and is also evident by the large positive damping coefficient (instability), starting around 925 RPM. Also marked on the damping plot is the rotor speed range over which the high loads event occurred – 920 to 940 RPM. The agreement between calculation and test data is excellent. Also marked on the figure is the region of ground resonance, which would occur at rotor speeds above 110% Ω_0. The general location of these instabilities agrees with the descriptions given in Ref. 27. Also, the stand frequencies were checked (before bolt replacement), and found to be at their original values. So, the event was caused by a shaft critical instability.
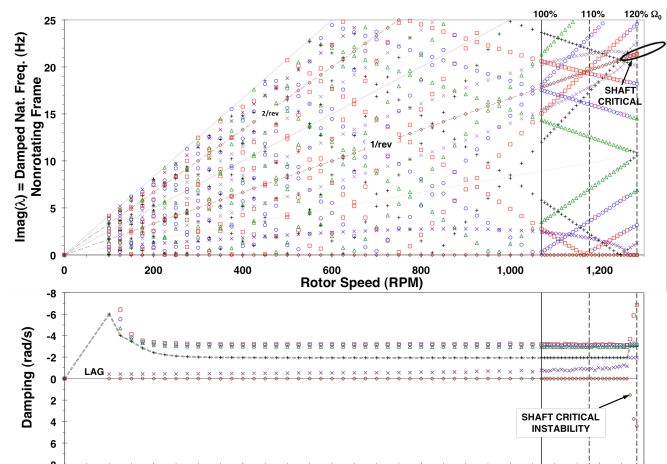

Figure 31. Aeromechanical stability (b=2), unbraced.

Although a shaft critical instability would not have occurred for a four bladed rotor, the ground resonance instability would have occurred at a lower rotor speed (Ref. 27). In fact, post event calculations showed that ground resonance would have occurred at Ω_0 (1,070 RPM) for the four bladed configuration. Consequently, some kind of system modification was needed, regardless of whether two or four blades were tested.

An effort to stiffen the stand was undertaken, that raised the fundamental stand modes to 36 Hz (lateral') and 39 Hz (longitudinal'), Table 4. This was accomplished by the addition of two diagonal braces (Figure 12 and Figure 13).

Aeromechanics calculations were performed, including a number of hypothetical perturbations. The calculations from one perturbation are shown in Figure 32 (2 blades), for which the stand frequencies were set at 90% of the braced values. This plot shows that the shaft critical instability has been moved well beyond 110% Ω_0. Calculations for four blades predict that ground resonance instability is moved above 120% Ω_0. Testing of AER on the braced ARTS – thru 103% Ω_0 (four blades) and Ω_0 (two blades) – confirmed the absence of aeromechanical stability problems.

Figure 32. Aeromechanical stability (b=2), 90% braced.

CAEA FLEXURE DEVELOPMENT & EXPERIENCE

Development. Flexure development is a challenging and critical process, that was performed by Domzalski Machine during the SBIR. Development included the testing of a variety of geometries and materials. The resulting design contains two custom, pre-cured laminates, subsequently bonded as an assembly, with the resulting link-flexure-elevon subassembly containing the flexure as a critical feature. In the region of the flexure, each laminate contains three plies of 1.45 oz industrial glass cloth. The 0°/90° cloth has its spanwise fibers removed (in the region of the flexure) via a manual process, and the remaining fibers are straightened. After impregnation with epoxy and curing, each laminate is 0.002 inch thick in the flexure region. After a quality assurance process, a pair of (cured) laminates are bonded together with a thin layer of elastomer. The center-to-center separation between the flexure laminates is 0.0085 inch, and the flexure chordwise length is 0.04 inch. Note that such light weight material and small dimensions increase the difficulty of flexure fabrication. The completed flexure region (Figure 29) contained six (chordwise) unidirectional glass/epoxy plies, three from each laminate, plus the thin layer of elastomer in the middle.

A single-wide assembly was fatigue tested on the bench, for an applied voltage of ±300 V, zero reaction load, and zero centrifugal force (CF). This electrical excitation produced a deflection of about ±10°, i.e. twice the design motion. At the time, the fatigue test was believed to capture the dominant fatigue loading of the assembly, including the

flexure. This specimen survived for 200 million cycles, and was believed to demonstrate good actuator system life.

Separate ultimate tests were performed for flexure laminate tensile strength, flexure shear strength, bond strength between the assembly and the blade, and a ground-air-ground fatigue test was performed for the bond between the assembly and the blade. Based on the flexure laminate tensile strength, along with measured blocked hinge moment and flexure geometry, the ultimate tensile strength was calculated to be 1.19 times the blocked force, for a design FS_u (tensile) = 2.38. This approach, of course, neglected the effects of CF and the compression strength.

Experience/rotor testing. After the two-bladed passive blade spin, another passive rotor test was conducted, this time with all four blades. The intent was to clear the envelope while work was being finished on the CAEA power system and control laws, demonstrating aeromechanical stability thru 103% Ω_0.

While testing at Ω_0 (1,070 RPM) and reducing the swashplate collective pitch angle, the rotor noise dramatically changed as -2° collective was approached, initiating an emergency shutdown. One inboard elevon (white control surface only) was found completely torn from its actuator, and another (the outboard elevon on the same blade) was found with upper fairing damage. Later testing revealed that the outboard elevon had a very low stiffness, as did one elevon on blade 4 (B4). Few elevon angle measurements were being recorded, but safety data from OBElvB1 indicated a maximum oscillation of about ±8° during the event. Prior to the event, the rotor had been tested at 2° collective thru 103% Ω_0, from 2° to 7.5° collective at 700 RPM, from 2° to 5° collective at 900 RPM, and up to 3° of cyclic pitch angle at 700 and 900 RPM, all without elevon actuation.

Subsequent analysis of the safety data and failed part yielded significant clues about the cause of the event. Although it is conceivable that some flexures were damaged during handling, no instances of pre-event abuse are known. An early hypothesis was that crossing zero thrust could cause high elevon motions due to wake impingement effects, but the data suggests this was not the root cause. The leading hypothesis, then, is that the flexures have inadequate strength margins and exhibit significant variations in their stiffness. (Stiffness variations are believed to be dominated by variations in the separation of the laminate-to-laminate centers.) Particularly compelling are the facts that IBElvB3 routinely showed a larger oscillatory motion (typically 2x to 3x) than OBElvB3 and that the blade 3 (B3) track was unusual. Unlike the shaft critical instability, this event produced large blade loads, but still no material limits were exceeded and the blades were undamaged, although some intact elevon flexures may have been damaged by large oscillations.

The leading failure scenario was hypothesized to occur in a few steps. First, elevon motion would degrade the flexure matrix (epoxy). This could be caused by unusually large motions due to handling or low stiffness (during rotor testing). It could also be caused by excessive epoxy on the exterior of the flexure and/or three-dimensional loading (especially at the ends of the flexure). Once matrix cracking is initiated, it will propagate thru the specimen. Then, once the matrix strength is lost, the shear strength of the flexure would be dramatically reduced. Next, a shear failure would occur. Bench test experience indicated that flexure failure normally occurs first in one laminate – starting at one end or the other – and that laminate fails completely before the second laminate fails. The failure of one laminate would greatly reduce the flexure bending stiffness, which could lead to large elevon motions and/or a change of the elevon frequency. This failure scenario is only hypothetical, but it is informed by a qualitative understanding of composite strength, some limited event data, and bench test experience with this particular flexure design.

The failure scenario is helpful because it highlights the possibility of frequency changes, which could change the extent to which the elevon couples with blade modes. This is potentially significant because it is conceivable that a degraded flexure would lead to an unfavorable coupling with a blade mode, causing high blade loads and potential blade loss. Such possibilities should be properly addressed and mitigated during future active rotor designs.

Examination of the failed flexure by a NASA Ames composites expert generated a number of suggested loading issues and potential remedies, encompassing design, materials, and manufacturing. The critical issue is that further development is needed – requirements definition, structural analysis, and testing. Efforts should be made to quantify and improve flexure structural margins, especially for a combined loading, fatigue environment. In addition, tighter control is needed of flexure stiffness, to improve the consistency of CAEA deflections (to commands and disturbances) and natural frequencies, and to reduce the possibility of excessive motions. A design trade should be conducted to determine a good balance between disturbance response and control response – perhaps a higher stiffness is needed. Improvements would be especially critical for full scale applications.

As a result of the failed flexure, a method was developed to measure the flexure stiffnesses. This technique was used before runs, and the stiffness trends were used to monitor flexure health. During all subsequent testing, to include the 2-bladed active rotor testing reported herein, no significant stiffness changes were observed. Nonetheless – because of the unknown fatigue strength of the CAEA flexures, the premature failure, and stiffness measurement scatter – the VSB-68 rotor balance was kept locked.

Blade 3 was repaired by the destructive removal of the two CAEAs, pocket clean-up, and installation of two spare

CAEAs. This process went very well and seems to have produced two healthy CAEAs. Since flexure stiffness testing found a soft flexure on Blade 4, a decision was made to perform the active rotor testing with only two blades. The blades selected for the active rotor test were Blades 1 and 2, which were placed in hub arms 1 and 3.

HOVER TEST MEASUREMENTS & OPERATIONS

Active rotor testing was performed for low collective pitch angles, from 2° to 5°. The nominal rotor speed was 1070 RPM (Ω_0), but significant testing was performed for a range of rotor speeds, between 0 and 103% Ω_0.

Blades 1 and 2 were used for the active rotor test, mounted in hub arms 1 and 3. A total of nineteen (19) strain gage bridges were installed on Blade 1 (B1) – nine (9) flap bending, four (4) chord bending, and six (6) torsion moment, as shown in Figure 2. (The most outboard torsion bridge did not survive the blade fabrication process.) Results are presented herein primarily for the three root (0.19 R) gages (FM01, CM01, and TM01), FM03 (0.24 R), TM03 (0.58 R), but also one figure for the full array of chord gages. Blade 2 loads data included only FM01 and TM01.

Elevon measurements were made on all four elevons with a Hall Effect (HE) transducer (on the blade) and magnet (on the elevon). Each elevon contained only one HE/magnet pair. OBElvB1 was measured on its outboard edge, but the other three elevons were measured on their inboard edge. For results presented in this paper, the elevons were operated in a collective (in-phase) mode, although some points were acquired for out-of-phase operation.

Additional deflection measurements included hub flap angle (B1 and B3) and lag angle (B1), blade root pitch angle (B1), and swashplate positions. The Pitch Horn Load was measured (B1). For active rotor testing, no rotor balance measurements were made – the balance was kept locked – although the rotor shaft torque was measured. The swashplate (fixed frame) lateral and longitudinal accelerations were measured. Actuator power records included the DC voltage commands and the HERO® Power Amplifier voltage and current monitor signals.

The signals were filtered by a variety of analog Bessel filters, with two or four poles, and a cutoff frequency of 600 or 1000 Hz. No filter corrections have been applied to the data.

Science data acquisition, elevon control, and some safety-of-flight monitoring ran on a Speedgoat real-time target machine (2.66 GHz core2-duo with 4 GB of memory). The user interface was implemented on a host computer (core i7-based) running Windows XP. The GUI application was built on Windows Forms technology, the .NET framework, and the National Instruments Measurement Studio development library. For this system, both the sample rate and control update rate were 4 kHz.

CONTROLS RESULTS

Before the controller results are shown, it is helpful to examine the characteristics of the disturbances observed in the hover chamber from an open-loop, 0V command condition. The rotor speed for the data presented here was 1070 RPM. Figure 33 shows the FFT of the data (no windowing applied) up to about 290 Hz. It is immediately obvious that the harmonics of the rotor frequency are the highest peaks, combined with some broadband disturbance. These two sources were approximately equal in magnitude contribution, with the harmonics adding slightly more than the broadband. The first 15 harmonics are clearly seen. This disturbance profile was used for post-test simulations.
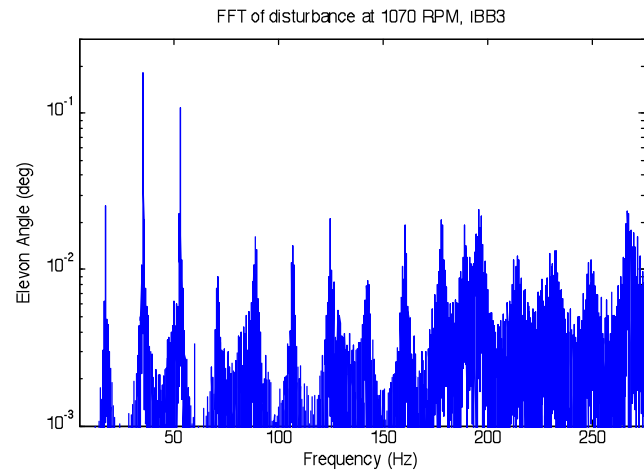
Figure 33. Frequency domain view of OL disturbance.

For the classical controller, stability and satisfactory margins and damping were achieved for all the elevons at the control design rotor speeds (0, 725, and 900 RPM). Performance results were of course a compromise resulting from the need to guarantee stability for all elevons in all conditions. Analyses indicated that while a crossover frequency of 208 rps (33 Hz) could be achieved for the inboard elevon of blade 1 at 725 RPM, only a crossover frequency of 163 rps (26 Hz) could be achieved for the inboard elevon of blade 3 at 900 RPM.

The final MPC controller provided stable control for all reference inputs (steady-state sinusoidal, frequency sweep, etc.), across all operating conditions (including 0 RPM and 1070 RPM), spanning all elevon assemblies. In simulation the crossover frequency was 204 rps (32 Hz) for IBB3 at 725 RPM and 327 rps (52 Hz) for IBB3 at 0 RPM. The 900 RPM condition had a an extremely low crossover frequency of approximately 70 rps (11 Hz) for IBB3. Gain margins were 5.4 dB in worst-case conditions (0 RPM) with all other conditions being far better. Worst-case phase margin was 56 degrees. Disturbance rejection bandwidth (-3 dB) was 163 rps (26 Hz) for 0 rpm condition and 128 rps (20.5 Hz) for 900 rpm condition.

Table 6 presents the performance metrics for the classical and MPC controllers based on analysis. The values

are averages over all the elevons and all RPMs. As may be seen, even though the two controllers followed completely different design approaches, the performance results are quite similar.

Table 6. Average controller performance (analysis).

	Crossover Frequency (rps)	-3 dB Ctrl Bandwidth (rps)	DRB (rps)
Classical	185	394	132
MPC	196	356	148

Figure 34 shows the 1-89 Hz closed-loop frequency sweep accomplished in experiment for both controllers. Unfortunately this sweep was performed at different rotor speeds for each controller; the classical controller was operating at the 900 RPM condition while the MPC controller was operating at the 1070 RPM condition. In simulation, both controllers were subjected to similar disturbance conditions found during the experiments (heavy disturbance on the harmonics, etc.) This disturbance is shown in simulation as 1070 RPM disturbance (1070d). Since a model for the 1070 RPM rotor speed condition was not generated, both simulated controllers were operating against the 900 RPM model that was previously discussed. For comparison, the simulated predictions for this situation are overlaid in dashed lines. The prediction does seem to represent the model accurately out to about 90 rps (14 Hz), but thereafter the predicted results diverge somewhat from the experimental results.
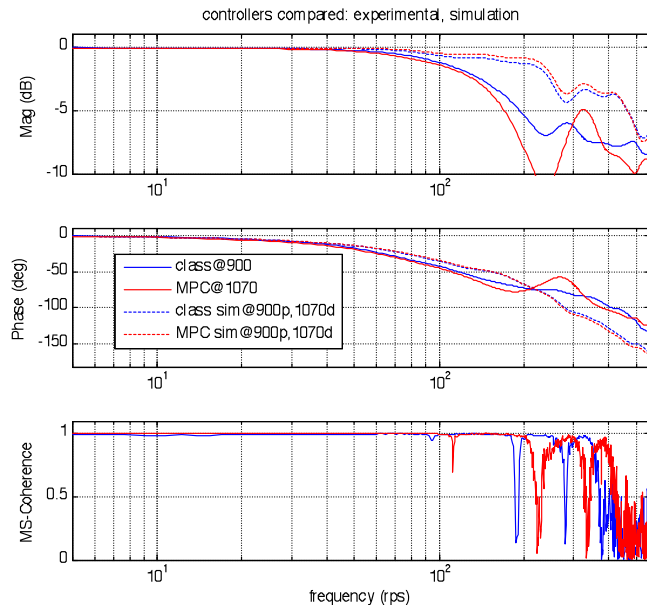
Figure 34. 1-89 Hz closed-loop response, exp/sim with disturbances.

Note that even though the predicted and experimental results diverge, the results for the two controllers track closely, both in simulation and in experiment. As may be seen from Figure 34, the experimental bandwidths are 153 rps for the classical controller and 143 rps for the MPC controller, which are quite comparable.

Comparing the experimental results with the numerical simulation results at higher frequencies yields Figure 35. This figure shows the comparison of IBB3 at 900 rpm. The plot is of a frequency sweep from 25 Hz to 275 Hz. There exists significant discrepancy between the simulated predictions and the experimental performance achieved. Also notice the coherence dipping at the harmonics of the rotor frequency. The cause of the discrepancy has not been determined.
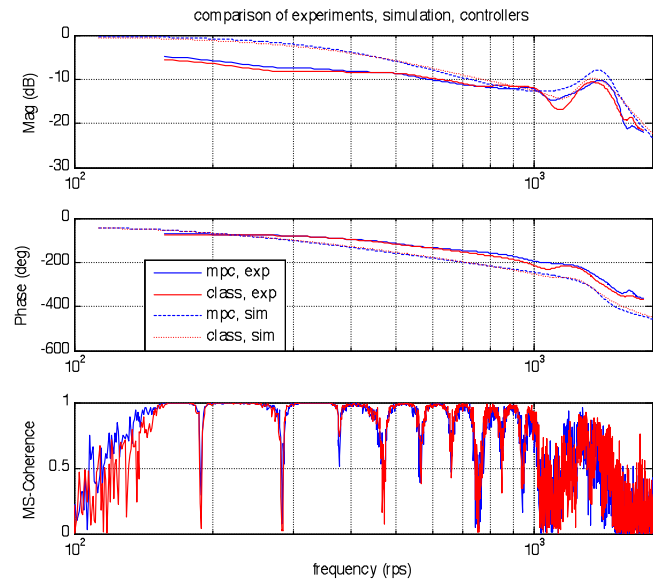

Figure 35. 25-275 Hz sweeps, exp/sim without disturbances.

Another useful metric for showing controller performance is comparing the reference signal to the measured output signal to form the error signal in the time domain. Figure 36 shows the reference signal at a steady-state frequency of 17.83 Hz and magnitude of 2 degrees. Since there was no project requirement for the phase shift, the measured output signal was advanced 32 samples (8ms, 51.35°) to understand how closely the reference magnitude and frequency were being followed. This signal shift value was determined by minimizing the standard deviation of the error signal over various signal advancement values. The final, lowest standard deviation was approximately 42% normalized error. The mean was very near 0°, which was expected.

While the absolute error is high, actually the reference tracking is doing well in terms of magnitude and frequency. The issues with absolute error are related to disturbance rejection of the controller, and this experiment had significant disturbance.

Displacement vs. Time
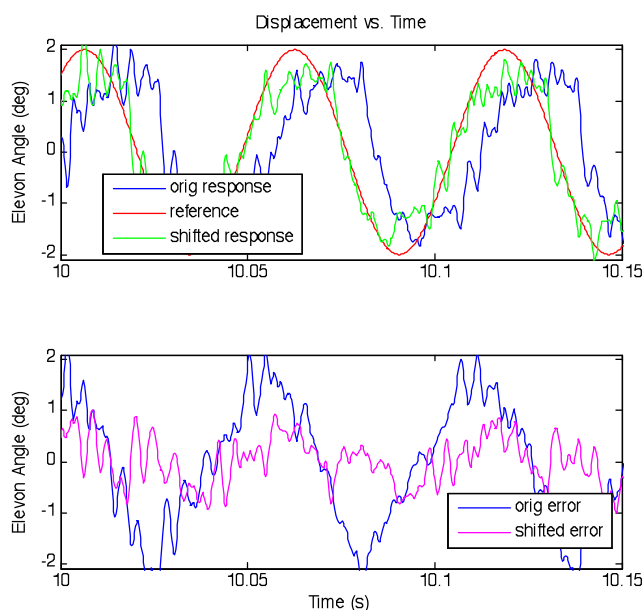
Figure 36. Steady-state error analysis for 17.83 Hz.

AEROMECHANICS RESULTS

CAEA Performance Overview

Although initial rotor testing used a CAEA oscillatory voltage limit of ±200 V (peak), based on bench test experience with the CAT actuators, it was found that the blade CAEAs could be successfully operated at higher voltages, up to ±300 V (peak). It is hypothesized that the batch of CAT actuators fabricated for bench testing had manufacturing defects not present in the production CAEAs. Nonrotating in situ tests of the blade CAEAs did exhibit electrical arcing (audible noise), even at oscillatory voltages below ±200 V. This arcing/noise suggests a latent deficiency (design or fabrication) or damage (from passive blade testing) of the production CAEAs.

The two-bladed active rotor was successfully tested up to full rotor speed (Ω_0 = 1070 RPM), full on-blade actuator electrical limits (±300 V), and low collective pitch angles (2°–5°). Significant testing was performed for a range of rotor speeds. The uncommanded steady elevon deflection was up to 2.5° at 1070 RPM (2° collective pitch). The commanded oscillatory (half peak-to-peak, hpp) elevon deflections were up to 3°/2.4° (IB/OB) thru 900 RPM, or 2°/1° (IB/OB) at 1070 RPM.

Frequency Dwells and Response

A variety of frequency dwells were conducted to quantify actuator and control performance for a range of discrete frequencies, and to obtain rotor response and elevon control authority data. In this section, all of the closed loop results used the MPC control algorithm. First will be a discussion of the elevon deflections, including magnitude, mean, and oscillatory (hpp) results. Second will be a discussion of the associated blade loads, that are indicative of modal participation and natural frequencies.

Elevon Deflections. A sinusoidal elevon motion was commanded at 7 Hz, and the elevon magnitude (at 7 Hz) is plotted in Figure 37, for a range of rotor speeds, both for open loop (75 and ~115 Vhpp) and closed loop (2°, MPC). The figure shows that each actuator had a different sensitivity to applied voltage (±75 V), but the trends with rotor speed are very similar. MPC was able to provide very accurate magnitude control for all elevons at 7 Hz, which indicates robustness of the controller. The open loop rotor speed trend – decreasing elevon oscillation for increasing rotor speed – was expected. This trend was likely caused by the dynamic pressure (q), since increasing q increases the (reaction) elevon hinge moment. Future work will be required to quantify the extent to which dynamic pressure explains the trend. An oscillatory elevon motion of ±2° was demonstrated thru 1025 RPM.
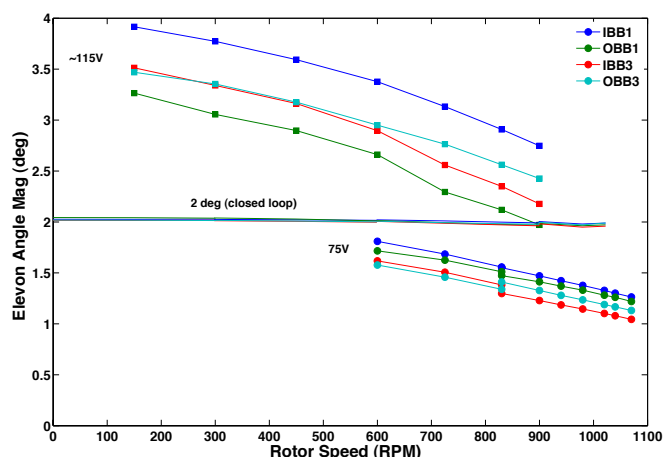
Figure 37. The effect of rotor speed on elevon deflection – 7 Hz response to 7 Hz voltage, for two open loop cases (75V and ~115V) and one closed loop case (2°).

The effect of rotor speed on the mean elevon angle is shown in Figure 38, both uncontrolled and controlled (MPC). Without actuation ("uncontrolled"), the trailing edge (TE) of all four elevons moved down (+ TE down) as the rotor speed increased. This trend was a surprise, since it was expected that each elevon would be in a region of positive lift, and the increasing dynamic pressure would force each trailing edge up. The most likely explanation is the -3° angle of the trailing-edge tab. Perhaps the observed trend is also influenced by an inertial effect, e.g. centrifugal force in the presence of coning (since the center of gravity of the elevon is aft of the hinge). Note that the rotor speed trends are generally similar, except for OBElvB1, which deflects most significantly to rotor speed changes. This sensitivity is likely caused by its relatively soft flexure, which was measured to be the softest of the four elevons. Note that the plotted mean angles are very significant, since the elevon design motion was ±5°. Note also that the four elevons have a range of deflections at 0 RPM. This indicates that some problem arose after fabrication – perhaps during rotor testing – since the as-fabricated static elevon positions were no more than ±0.35 deg. Also, note that the mean angle was very well controlled by MPC – all four elevons appear to be a single,

straight, horizontal line. This control, of course, came at the price of actuation voltage (not shown), thus reducing the voltage available for dynamic actuation. One strategy for reducing the severity of the voltage constraint is to allow a nonzero mean elevon angle. This strategy was used for a few test conditions (not shown), since it might be a good trade in some circumstances.
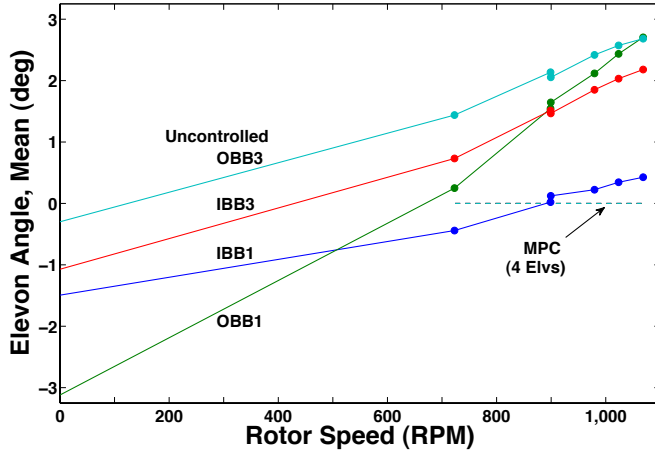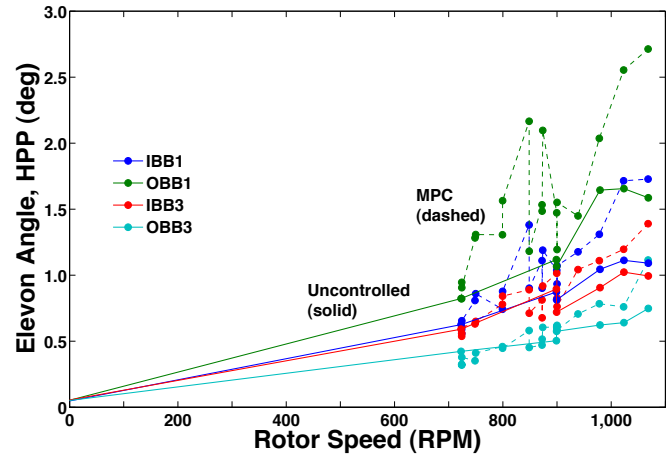

Figure 38. Effect of rotor speed on mean elevon angle, uncontrolled and 0 mag controlled (MPC).

The effect of rotor speed on the oscillatory (hpp) elevon angle is shown in Figure 39, both uncontrolled and controlled (MPC), with the latter using a 0° command (i.e. 0 mag control). Included in the figure are a number of repeat points, which reveal significant scatter in the data. The hpp oscillation was calculated for each data point, based on the minimum and maximum values captured during the data point. Note that, whereas the uncontrolled data points used a 30 second duration, the MPC data used a 6 second duration except for the highest three rotor speeds and one of the 900 RPM points, all of which used a 30 second time record. Also, note that a variety of experimental evidence indicated the significant effect of disturbances (presumably due to recirculation), including significant transients (perhaps due to gusts and unsteady wake effects). The transients caused significant changes in the oscillatory blade loads and elevon deflections over relatively long periods, e.g. 15 to 60 seconds. Although a statistically precise analysis would require more data than was acquired, the trends shown in Figure 39 provide a first order understanding of the unsteady elevon motion.

Figure 39 also shows that OBElvB1 (green) had the largest oscillatory motion of the four elevons, which is consistent with it having the smallest flexure stiffness. In Figure 39, OBElvB1 had an oscillatory motion as large as 1.7° (uncontrolled) or 2.7° (MPC) hpp. Note also that the oscillations measured for MPC are generally significantly larger than the uncontrolled oscillations. The extent to which the disturbance is increased is in general agreement with the predicted MPC disturbance magnitude peak of 4.5 dB or about 67%. Thus, it appears that the DRB (disturbance rejection bandwidth) of the implemented MPC

algorithm was inadequate for precise position control with such a large disturbance. In particular, note that the plotted oscillations are very significant, since the elevon design motion was ±5°. More significantly, this data suggests that some additional actuator design requirement may be needed – e.g. to stiffen the elevon flexures and increase the elevon damping near resonance – to reduce the magnitude of the uncommanded oscillations.

Figure 39. Effect of rotor speed on oscillatory (hpp) elevon angle, uncontrolled and 0 mag controlled (MPC).

Results from closed-loop (MPC) elevon amplitude sweeps are given in Figure 40 thru Figure 42, for 900 RPM. Figure 40 compares the measured elevon magnitude with the commanded magnitude, for 4 and 39 Hz. As expected, the results at 4 Hz are excellent, since this frequency is well below the control bandwidth. The results at 39 Hz, however, show significant attenuation and larger variation between the four elevons, since this frequency is above the control bandwidth. IBElvB3 has the smallest response.
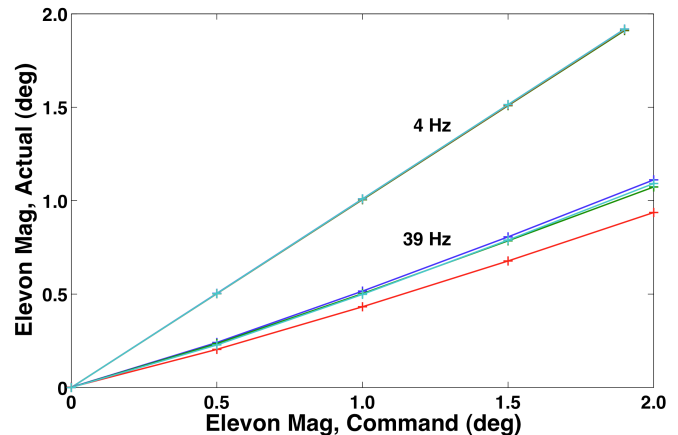
Figure 40. Correlation between commanded and measured elevon magnitudes, all four elevons, 900 RPM – 4 and 39 Hz.

Blade Loads. The associated trends for blade moments (flap, chord, and torsion; in-lb; B1 root) are shown in Figure 41 (4 Hz) and Figure 42 (39 Hz). (Here the abscissa is an average of the inboard and outboard elevon measurements from

blade 1.) Note that 4 Hz is the frequency of the first lag mode (ζ_1), and 39 Hz is the frequency of the second flap mode (β_2). As expected, a comparison of the two figures reveals that the largest structural moment (at the blade root) corresponds to the mode definition. Furthermore, the flap and torsion moments have significantly increased at 39 Hz, although the chord moment has a similar magnitude (about 10 in-lb for 1.1° elevon magnitude). In each figure, the dominant response is essentially linear, and the torsion moment shows very low response for the smallest elevon magnitude increment (0.50° or 0.25°). For 39 Hz, the secondary responses (torsion and chord) have a reducing sensitivity (smaller slopes) as the elevon magnitude increases. Although the elevon angles are relatively small, these structural loads exhibit clear trends.
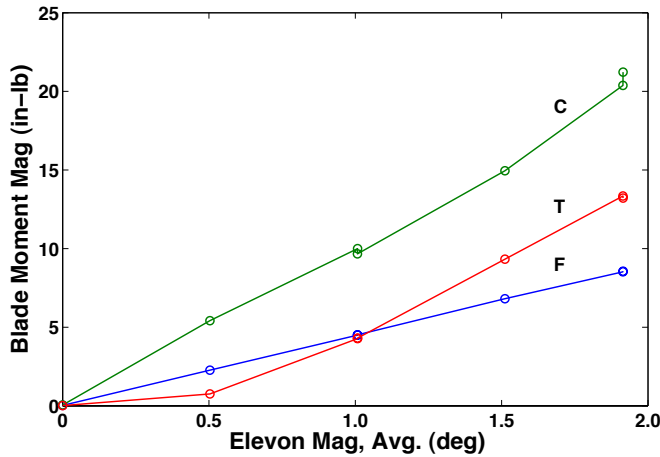
Figure 41. Blade load trends with elevon deflection, 900 RPM, B1 root – 4 Hz (ζ_1).
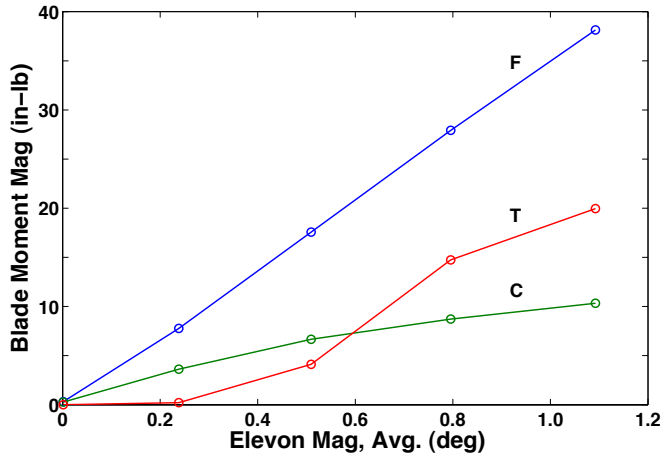

Figure 42. Blade load trends with elevon deflection, 900 RPM, B1 root – 39 Hz (β_2).

The effect of rotor speed on blade moments (flap, chord, and torsion; blade 1 root) is shown in Figure 43, for commanded elevon motion of 2° at 7 Hz (MPC), with all elevons commanded in a collective ("in-phase") mode. The flap bending moment (FM) magnitude shows a minimum around 600 RPM, indicating that this is the elevon reversal speed. The reason for the local peak in the torsion moment

(TM) is unknown. Repeat points acquired at 300, 600, and 900 RPM show the scatter to be relatively small, most prominent for the chord bending moment (CM) at 900 RPM.
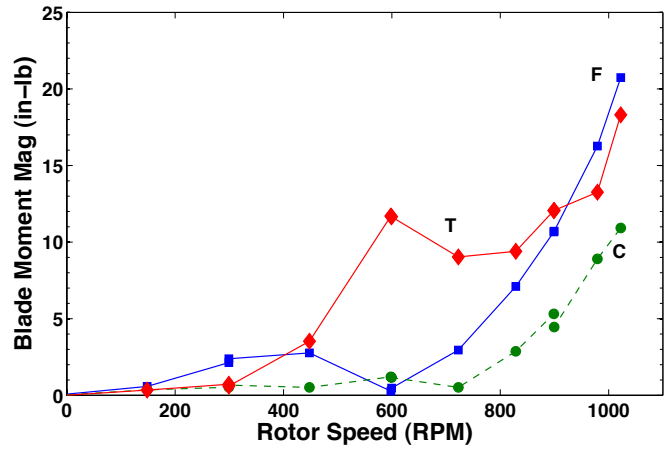

Figure 43. The effect of rotor speed on blade moments (B1 root), 2° elevon oscillation – 7 Hz.

Frequency dwells were performed for select frequencies, in the vicinity of blade modes at 900 RPM. Frequencies were selected from modal peaks from frequency response functions (FRFs, discussed later) and pre-test predictions. Results for the blade loads (B1 root) are shown in Figure 44. Note that the delta magnitude (dMag) is plotted, obtained by subtracting the (relatively small) 0V magnitudes (at each frequency) and then normalizing by the average elevon deflection magnitude. Solid lines are used to show the general trends, although the small number of frequencies means that the resulting curves can not be used to quantify resonant amplification or damping. Nonetheless, some significant peaks are evident, in the vicinity of the tested points, suggesting the approximate location of some blade modes, especially lag 1 (ζ_1), flap 2 and 3 (β_2 and β_3), and torsion 1 (ϕ_1).
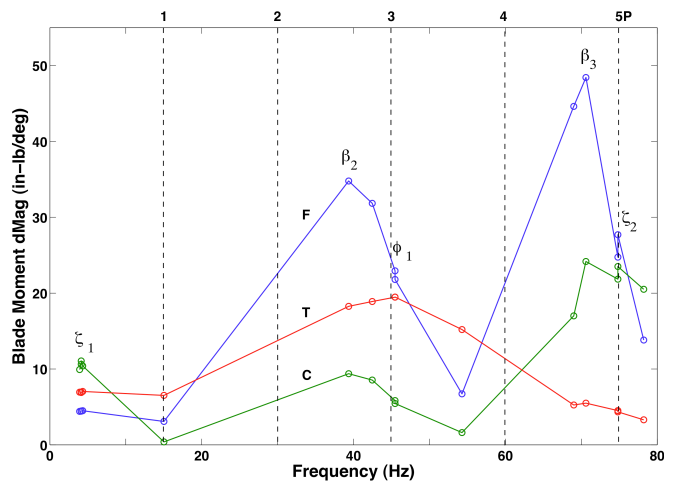

Figure 44. Blade load trends with elevon frequency, B1 root, 900 RPM.

Note that ϕ_1 appears to be close to 3/rev (45 Hz), and that the predicted frequency (54 Hz) is too high. This

discrepancy is large and quite significant. Note also that the ζ_2 prediction (78 Hz) is also too high, since the actual mode is in the vicinity of 5/rev (75 Hz). Additional discussion of the blade frequency identification will be provided later. For now, note that several frequencies remain uncertain – flap 1 (β_1), torsion 1 (ϕ_1), and lag 2 (ζ_2) – although it is clear that ϕ_1 and ζ_2 are significantly lower than predicted. To obtain a more precise determination of the blade frequencies using frequency dwells, additional frequency test points would be needed. Instead, significant test time was devoted to frequency sweeps, which are discussed in the next section.

Blade Load FRFs

Logarithmic frequency sweeps were conducted over a wide frequency range, to facilitate the identification of blade modes, elevon dynamic response, and elevon control authority, from frequency response functions (FRFs). Here, the FRFs have elevon angle as the input, and a blade load (e.g. flap bending moment) as the output, with magnitude units of in-lb/deg, expressed in dB. Of immediate interest was the determination of blade natural frequencies and actuator performance. If the quality of the FRFs allowed, perhaps the damping could be determined for a few blade modes. To date, though, no attempt has been made to calculate the damping of blade modes. In this section, the results and discussion are limited to blade frequencies.

The torsion moment FRF – magnitude, phase, and coherence – is shown in Figure 45 for 1–89 Hz elevon motion, TM03 (blade 1), for collective ("in-phase") elevon motion, at three rotor speeds: 725, 900, and 1070 RPM. Here, the elevon "input" is the average of the measured inboard and outboard elevon angles. A few significant details are evident in this figure. First, the steady-state response is of excellent quality (high coherence); the magnitude increases with rotor speed; and the steady-state phase is about -180°. The phase angle means that the blade root section is experiencing a nose-down (negative) torsion moment for trailing-edge down (positive) elevon deflection, as was expected from the pitching moment induced by elevon deflection. Second, note that the phase and magnitude responses generally indicate that the torsion moment is dominated by a single mode, ϕ_1. These trends, though, are somewhat obscured by deviations caused by the disturbance (recirculation, etc.). Third, the coherence shows significant "per rev valleys", or rapid drops in proximity to harmonics of the rotor speed (1/rev). Most evident are the drops at 2/rev (24 Hz at 725 RPM, 30 Hz at 900 RPM, and 36 Hz at 1070 RPM).

Note especially (Figure 45) the correspondence between the 1070 RPM (2/rev, 36 Hz) coherence drop and the phase and magnitude deviations, and to a lesser degree the effect on the 900 RPM response (30 Hz). (An attempt to fit this data with a model has not yet been made, although the effort may be complicated by the per rev valleys, which are more significant for flap and chord bending.) For the torsion response shown here, simple interpretation is hindered by

the relatively small input and large disturbance. For example, the shape of the resonant peak at 725 RPM is unusual, since it is near 4/rev. For 1070 RPM, the (magnitude) peak near 27 Hz appears to be an artifact of the nearby 2/rev coherence drop; instead, the true resonant peak (ϕ_1) is likely near 43 Hz, observable because of its reasonable separation from per rev contamination. Preliminary examination of the data was performed using heuristics such as these, mainly to tabulate those frequencies that could be reasonably identified from a good magnitude peak.
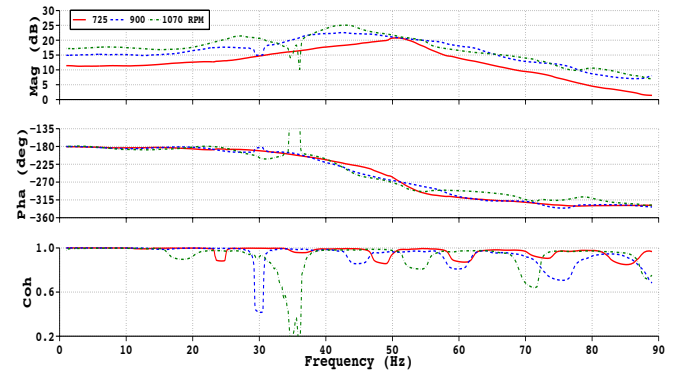
Figure 45. Torsion moment (TM03) FRFs: 725, 900, and 1070 RPM.

The corresponding FRFs for the flap bending moment are shown in Figure 46, for the same three rotor speeds: 725, 900, and 1070 RPM. The coherence indicates significantly reduced quality relative to the torsion moment FRFs. Nonetheless, the quality of the steady-state results are still very good except for 1070 RPM, which has a decreasing coherence for very low frequencies. The steady-state magnitude increases with rotor speed, and the phase starts around -180° since all of these speeds are higher than the elevon reversal speed (Figure 43). For these three FRFs, then, the blade lower surface is in compression (negative flap bending moment) due to positive elevon deflection (trailing edge down) for low frequencies. This is consistent with the sign of the (steady state) blade lift being dominated by (nose down) blade twist; that is, changes in the blade angle of attack have overpowered elevon direct lift.
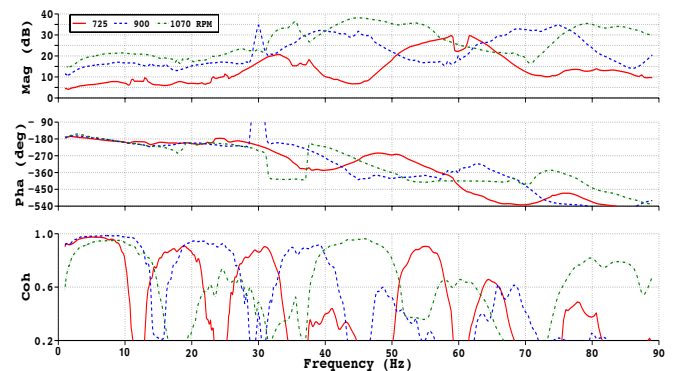
Figure 46. Flap bending moment (FM03) FRFs: 725, 900, and 1070 RPM.

For flap bending moment (Figure 46), significant coherence valleys are evident starting at 1/rev (12 Hz at 725 RPM, 15 Hz at 900 RPM, and 18 Hz at 1070 RPM). The first flap bending mode (β_1) should be near 1/rev but is not clear in these FRFs, likely due to the high damping (low response). The second mode (β_2), however, is evident – rising from 33 Hz at 725 RPM, to 39 Hz at 900 RPM, and finally to 47 Hz (1070 RPM) – with the most accurate of these peaks being the one at 1070 RPM. The general rise of the β_3 frequency with rotor speed is also apparent in the figure. One prominent peak defect is evident in the figure – the β_3 peak near 60 Hz for 725 RPM – due to a 5/rev valley.

Another investigative approach is to study the FRFs at one rotor speed, using all available blade load measurements, pitch horn loads, and the hub deflection measurements. An example is given in Figure 47, which shows the chord bending magnitude FRFs from all four chord bending moment bridges and the hub lag angle (multiplied by 1000), at 1070 RPM. Also marked on the plot are the /rev lines for this rotor speed. The plot indicates strong resonant responses at the first and second lag modes (ζ_1 and ζ_2) and appreciable modal participation around 2.5/rev (the vicinity of β_2 and ϕ_1).

In addition to plots like Figure 47, that focus on a single loading direction (flap, lag, or torsion), a few plots were combined to show all three loading directions, to determine the dominant contributor to a particular modal frequency.
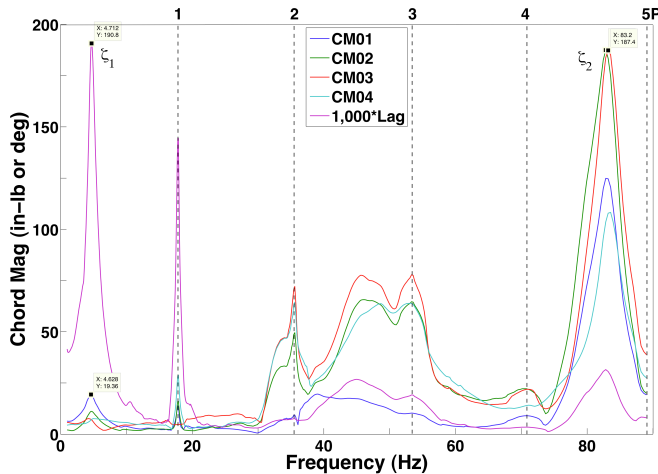

Figure 47. FRF magnitudes of the chord bending moment at four STAs and lag angle, 1070 RPM.

Blade Frequencies

Preliminary blade frequencies were obtained from the magnitude peaks of select FRFs, as discussed above. Furthermore, the results at 900 RPM were checked against the frequency dwell results (Figure 44). Figure 48 shows a summary of the experimental frequencies (symbols) along with pre-test calculations (lines). The test data matches the calculations quite well for the first lag mode (ζ_1) and second flap mode (β_2), and reasonably well for the third flap mode

(β_3) and second lag mode (ζ_2). The first flap mode (β_1) was not accurately identified. The agreement for the first torsion mode (ϕ_1) is very poor. The ϕ_1 frequency difference is 0.3/rev at 725 RPM, but the difference increases to 0.7/rev at 1010 RPM. The leading hypothesis for this difference – at least at 725 RPM – is unmodelled swashplate compliance (that has not been measured). Three of the experimental frequencies have been marked with a gray interior to indicate their relative uncertainty – ϕ_1 and ζ_2 at 900 RPM, and β_1 at 1070 RPM. Significant work remains to develop a more accurate identification of the blade frequencies, and to determine why the calculations differ from the test data.
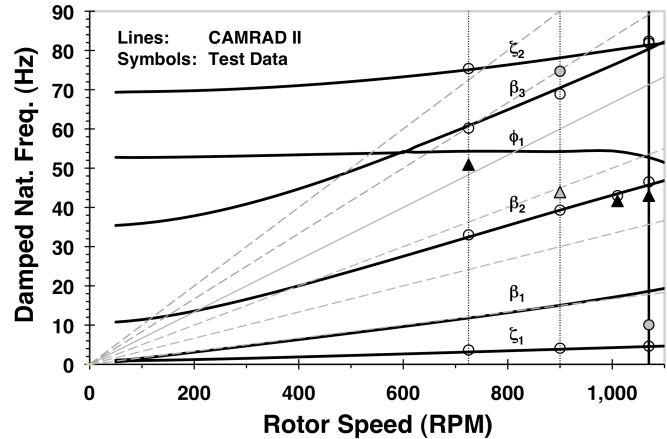

Figure 48. Variation of damped natural frequencies with rotor speed – numerical predictions and test data.

FUTURE WORK

An explicit model of the disturbance (or possibly even a robust online disturbance ID system) should be developed, since MPC should gain significant DRB improvements if such a model can be known accurately. In this same vein, a robust, adaptive plant identification algorithm could lead to improved performance across varying actuators without making the compromises inherent in a fixed model of the plant.

Another aspect that could be improved in the future is the plant model and finding a more accurate non-linear representation so that more capable, high-performance controllers can be developed through more accurate simulation and optimization.

To more precisely quantify the blade modes, additional analysis should be performed. For example, if transfer function models could be successfully fit to the experimental FRFs, then the models could provide both frequency and damping for several blade modes. Such an effort is believed worthwhile, especially to better quantify the first torsion mode (ϕ_1). In addition, it is possible that an analysis of the blade mode shapes would provide a physically meaningful basis for comparison with calculations. Analysis of the relative difference between the IB and OB elevon control authorities is also warranted.

Initial plans were for the AER hardware to be tested in a wind tunnel in forward flight, but there are currently no plans for further testing of this rotor system. To evaluate the ability of the elevons to reduce vibratory hub loads in forward flight, additional analysis is required. Since a significant distribution of strain gages were used for AER, the structural loads could be integrated to estimate the blade forces (shears) acting on the hub.

CONCLUDING REMARKS

Development and hover testing of the Active Elevon Rotor (AER) has been completed. The paper included two main parts: 1) development, and 2) testing and results. Development included the completion of the Army Rotorcraft Test Stand (ARTS), an articulated hub, the actuators and CAEAs (Conformal Actuator and Elevon Assemblies), the CAEA power system, two control algorithms, and the AER blades. Key development efforts and technical issues were described, along with their resolution and suggestions for future work.

Testing and results were described for a variety of systems, especially the actuators, the CAEAs, two control laws, and the rotor. Testing included actuator and CAEA bench tests, aerodynamic testing of the CAEA, and rotor testing. Initial results were described for the performance of the CAEAs, control laws, aeromechanics stability, and the aeromechanics response and characteristics of the AER blades.

The reliability of the CAT actuators (bench test articles) was poor for oscillatory voltages above ±40 V/mil, although the production blade CAEAs (actuator assemblies) performed well up to about ±60 V/mil. These electric field limits, though, are only approximate because of the small number of specimens, varied test conditions, and short rotor test time. It is clear, though, that the actuators did not consistently meet the design goals, and that additional work is needed to quantify and improve CAT reliability.

The two-bladed active rotor was successfully tested up to full rotor speed (Ω_0 = 1070 RPM), full on-blade actuator electrical limits (±300 V), and low collective pitch angles (2°–5°). Significant testing was performed for a range of rotor speeds. The uncommanded steady elevon deflection was up to 2.5° at 1070 RPM (2° collective pitch). The commanded oscillatory (hpp) elevon deflections were up to 3°/2.4° (IB/OB) thru 900 RPM, or 2°/1° (IB/OB) at 1070 RPM. The control bandwidth was 1.3/rev, significantly below the goal of 5/rev for closed-loop control of the CAEA.

Elevon oscillation of ±2° was demonstrated at 7 Hz thru 1025 RPM for all four elevons. The design motion (±5°) was not achieved for two main reasons: 1) actuation voltage was expended to zero the mean elevon angles, and 2) elevon peak deflections included significant uncommanded motions due to unsteady loads (presumably due to recirculation). Although a more complete demonstration would require the

elimination of one or both of these issues, the voltage sensitivity of the CAEAs was very good.

The elevon was able to excite a few blade modes sufficiently well for the identification of the associated frequency – especially ζ_1, β_2, and β_3 – along with tentative frequencies for ϕ_1 and ζ_2.

Particularly noteworthy accomplishments include the following:

1. Two separate controllers, one using classical control approaches and another using Model Predictive Control, were developed. The performance goals for the controllers were achieving the best control and disturbance rejection bandwidths possible while maintaining stability and adequate margins in the presence of the lightly damped primary resonance mode of the elevons. The two controllers, arrived at using two disparate approaches but controlling the same system toward the same set of performance goals, achieved quite similar results in terms of overall performance, both in analysis and in actual experiments.

2. Even though the analyses showed that both controllers should be able to achieve relatively high control bandwidths (close to 400 rps or 3.5/rev), the actual bandwidths observed in the hover chamber were significantly lower (around 150 rps or 1.3/rev). The cause of this discrepancy has not been determined but the two controllers exhibited very similar performance characteristics, even in the hover chamber.

3. There is a significant difference – from 0.3/rev (725 RPM) to 0.7/rev (1010 RPM) – between the predicted and measured first torsion (ϕ_1) frequencies. Swashplate assembly compliance should be measured, and an updated analysis should be conducted.

4. Uncommanded elevon oscillation and mean angle variation with RPM were very significant. Future consideration should be given to appropriate design requirements for elevon flexure stiffness and damping, especially for increased control bandwidth and reduction of uncommanded deflections for potential forward flight applications.

5. Elevon flexure design and analysis need to be improved, especially for fatigue strength, robustness, and consistency of bending stiffness. More generally, detailed analysis of the CAEA is needed. A larger scale application would facilitate the use of more optimal materials and closer tolerances.

6. Structural failure of the elevon flexure may be relatively gradual, resulting in a reduction of the fundamental elevon frequency, from its design value to a very low value, crossing a wide range of frequencies and blade

modes. There is a potential for interaction of a degraded elevon frequency with a blade frequency, possibly increasing the blade loads by a significant amount. Active rotors with similar failure modes should analyze the likely consequence of such failures, including the possibility of excessive blade loads, flutter, and blade loss.

Development and hover testing of AER/ARTS has demonstrated important new test capabilities in a challenging environment. Significant data was obtained about system performance, sparking recommendations for future work. Initial study of the aeromechanics data has shown it to be of good quality and has identified significant blade frequencies.

ACKNOWLEDGMENTS

REFERENCES

[1]Wood, E.R., Powers, R.W., Cline, J.H., and Hammond, C.E., "On Developing and Flight Testing a Higher Harmonic Control System," *Journal of the American Helicopter Society*, Vol. 30, (1), January 1985.

[2]Arnold, U.T.P., "Recent IBC Flight Test Results from the CH-53G Helicopter," 29th European Rotorcraft Forum, Friedrichshafen, Germany, September 2003.

[3]Norman, T.R., Theodore, C., Shinoda, P., *et al.*, "Full-Scale Wind Tunnel Test of a UH-60 Individual Blade Control System for Performance Improvement and Vibration, Loads, and Noise Control," Proceedings of the 65th Annual Forum of the American Helicopter Society, Grapevine, Texas, May 2009.

[4]Fulton, M.V. and Ormiston, R.A., "Hover Testing of a Small-Scale Rotor with On-Blade Elevons," *Journal of the American Helicopter Society*, Vol. 46, (2), April 2001.

[5]Fulton, M.V. and Ormiston, R.A., "Small-Scale Rotor Experiments with On-Blade Elevons to Reduce Blade Vibratory Loads in Forward Flight," Proceedings of the 54th Annual Forum of the American Helicopter Society, Washington, DC, May 1998.

[6]Dieterich, O., Enenkl, B., and Roth, D., "Trailing Edge Flaps for Active Rotor Control – Aeroelastic Characteristics of the ADASYS Rotor System," Proceedings of the 62nd Annual Forum of the American Helicopter Society, Phoenix, Arizona, 2006.

[7]Straub, F.K., Anand, V.R., Birchette, T.S., and Lau, B.H., "Wind Tunnel Test of the SMART Active Flap Rotor," Proceedings of the 65th Annual Forum of the American Helicopter Society, Grapevine, Texas, May 2009.

[8]Lorber, P.F., O'Neill, J.J., Andrews, B.I.J., *et al.*, "Whirl Test of a Large Scale High Authority Active Flap Rotor," Proceedings of the 66th Annual Forum of the American Helicopter Society, Phoenix, Arizona, May 2010.

[9]Wilbur, M.L., Yeager, W.T., Jr., Sekula, M.K., "Further Examination of the Vibratory Loads Reduction Results from the NASA/Army/MIT Active Twist Rotor Test," Proceedings of the 58th Annual Forum of the American Helicopter Society, Montréal, Canada, June 2002.

[10]Fulton, M.V., "Design of the Active Elevon Rotor for Low Vibration," American Helicopter Society Aeromechanics Specialists' Meeting, Atlanta, Georgia, November 2000.

[11]Fulton, M.V., "Aeromechanics of the Active Elevon Rotor," Proceedings of the 61st Annual Forum of the American Helicopter Society, Grapevine, Texas, June 2005.

[12]Shin, S., Cesnik, C.E.S., and Hall, S.R., "Closed-Loop Control Test of the NASA/Army/MIT Active Twist Rotor for Vibration Reduction," Proceedings of the 59th Annual Forum of the American Helicopter Society, Phoenix, Arizona, May 2003.

[13]Hall, S.R., Anand, V.R., Straub, F.K., and Lau, B.H., "Active Flap Control of the SMART Rotor for Vibration Reduction," Proceedings of the 65th Annual Forum of the American Helicopter Society, Grapevine, Texas, May 2009.

[14]Straub, F.K., and Johnston, R.A., "Aeroelasticity and Mechanical Stability Report, 0.27 Mach Scale Model of the YAH-64 Advanced Attack Helicopter," NASA CR 178284, May 1987.

[15]Domzalski, D.B., "Deformable Trailing Edges and Smart Material Actuation for Active Control of Rotor Blades," Presented at the Ninth International (ARO) Workshop on Aeroelasticity in Rotorcraft Systems, University of Michigan, October 2001.

[16]Domzalski, D.B., "Deformable Trailing Edges and Smart Material Actuation for Active Control of Rotor Blades," Phase II SBIR Final Report, USAAMCOM TR 02-D-19, Contract No. DAAH10-99-C-0022, March 2002.

[17]Johnson, W., "Rotorcraft Dynamics Models for a Comprehensive Analysis," Proceedings of the 54th Annual Forum of the American Helicopter Society, Washington, D.C., May 1998.

[18]Johnson, W., "Rotorcraft Aerodynamics Models for a Comprehensive Analysis," Proceedings of the 54th Annual Forum of the American Helicopter Society, Washington, D.C., May 1998.

[19]Petot, D., "Differential Equation Modeling of Dynamic Stall," La Recherche Aerospatiale, No. 1989-5, 1989.

[20]Wong, R.L., "CFD-Based Predictions of Rotor Elevon Effectiveness," M.S. Thesis, University of California, Davis, Dept. of Mechanical and Aeronautical Engineering, 2002.

[21]Tischler, M.B. and Remple, R.K., *Aircraft and Rotorcraft System Identification: Engineering Methods with Flight Test Examples*, 2nd Edition, AIAA, Forthcoming.

[22]Blanken, C.L., Hoh, R.H., Mitchell, D.G., and Key, D.L, "Test Guide for ADS-33E-PRF," U.S. Army RDECOM special report AMR-AF-08-07, July 2008.

[23]Tischler, M.B., *et al.*, "A Multidisciplinary Flight Control Development Environment and Its Application to a Helicopter," *IEEE Control Systems Magazine*, Vol. 19, (4), pg. 22-23, August 1999.

[24]Wang, Liuping., *Model Predictive Control System Design and Implementation Using MATLAB*, Springer, 2009.

[25]Rossiter, J.A., *Model-Based Predictive Control: A Practical Approach*, CRC Press, 2004.

[26]Geissler, W., "Dynamic Stall Control by Static Flap Deflection," Final Technical Report to the European Research Office of the U.S. Army, Contract No. N68171-00-M-5987, DLR Report No. IB 224 - 2002 C 07, September 2002.

[27]Johnson, W., *Helicopter Theory*, Dover Publications, Inc., New York, section 12-4.4, pp. 685–693, 1994.